UNIVERSITÀ
DEGLI STUDI
DI PADOVA

Dipartimento di Ingegneria dell'Informazione

Corso di Dottorato in Ingegneria dell'Informazione

Curriculo: Bioingegneria

Ciclo XXIX

# Correction of distortions in MR Echo Planar images using a super-resolution T2-Weighted volume

**Coordinatore:** Prof. Matteo Bertocco

**Relatore:** Prof. Alessandra Bertoldo

**Dottorando**: Andrea Nordio

# CONTENTS

# Introduction

Magnetic resonance imaging (MRI) is a widely used technique to assess brain diseases without the use of ionizing radiations. Brain anatomy can be captured using T1-Weighted (T1W) and T2-Weighted (T2W) acquisitions. T1W are used to differentiate brain tissues mainly on the basis of T1 value. Tissues with high fat content (e.g. white matter) appear bright, while tissues with high concentrations of water (e.g. cerebrospinal fluid) appear dark. T2W sequences differentiate tissues mainly on the basis of T2 value. They are acquired for their excellent tissue contrast between gray and white matter, and typically they have a resolution in-plane very high (much higher than the through-plane one, due to SNR and acquisition time problems). In T2W compartments filled of water appear bright, while structures with high fat content appear dark. Since most of the brain lesions are associated with an increase in water content, T2W images are really helpful for demonstrating pathologies. In addition to mapping brain anatomy, MRI can be also applied to study the brain functions or the grey-white matter connections. Tissue perfusion can be assessed with magnetic labeling of arterial spins [1] or with the intravenous injection of a bolus of paramagnetic contrast agents [2]. Structural information of the brain can be assessed by using Diffusion Weighted Imaging (DWI) and Diffusion Tensor Imaging (DTI) techniques, which measure the Brownian motion of water molecules in tissues [3], while MR Spectroscopy (MRS) provides a measure of brain chemistry [4]. The basic principle of MRS is that the distribution of electrons around an atom cause nuclei in different molecules to experience a slightly different magnetic field. This results in slightly resonant frequencies, which in turn return a slightly different signal. MRI can also indirectly detect changes in brain activity measuring the changes in Blood Oxygenation Level Dependent (BOLD) contrast [5]. Since neurons do not have internal reserves of energy, their firing causes a need for more energy to be brought in quickly. Through a process called the hemodynamic response, blood releases oxygen to neurons at a greater rate than to inactive neurons: this causes a change of the relative levels of oxygenated and deoxygenated blood, i.e. a change of the contrast between the two level of blood oxygenation that can be detected on the basis of their differential magnetic susceptibility. This acquisition technique is called functional Magnetic Resonance Imaging (fMRI), and it represents an indirect measure of the neuron activity.

The examination of brain BOLD signal by fMRI has led to a revolution in neuroscience over the last decades. Figure 1 shows the number of publications per year found using the keywords “fmri AND brain” (source: Pubmed): in the plot a growing interest in this field is shown by the trend of publications in the last years.

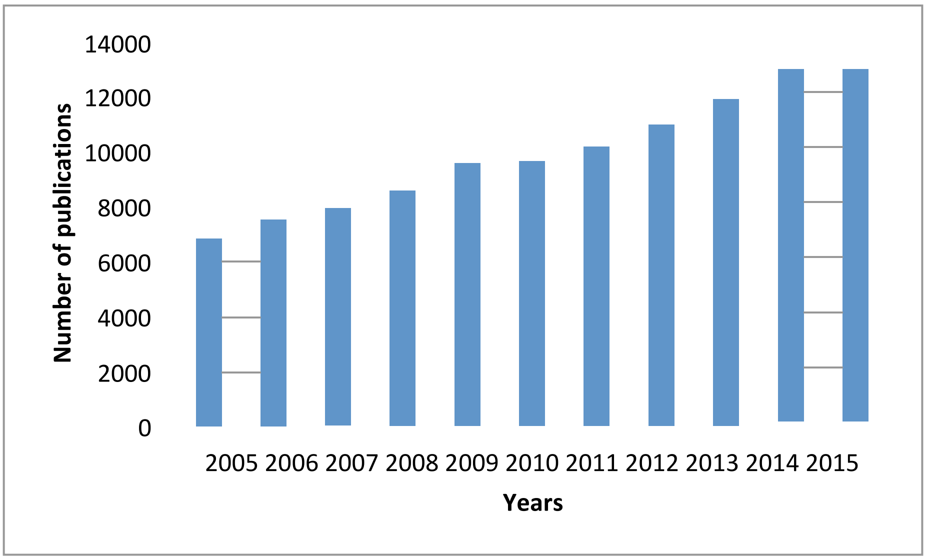

**Figure 1 - Trend of the number of publications per year using the research words "fMRI AND brain" in Pubmed**

Although BOLD-based techniques have been shown to work reliably for a huge range of applications, straight-forward BOLD imaging has some inherent problems [5], first of all the low signal to noise ratio (SNR). The analysis of fMRI datasets requires some preprocessing step including the realignment of volumes, the distortions correction, the temporal and spatial filtering. One of the most common source of noise is the motion of subjects [7]: these movements induce spin-history artifacts and motion-by-susceptibility interactions [8]. Eye movements, as well as movements of the tongue or lower jaw, can alter the homogeneity of the magnetic field and introduce distortions in the images [9,10,11]. A second source of noise is the presence of physiological processes like breathing or heart beat [12,13], which can vary from dataset to dataset. One of the main artifacts are the macroscopic field inhomogeneity effects that produce spatial distortions in the acquisitions [14]. These distortions especially occur at the interface between soft tissues and air, for example in the frontal and supra-temporal regions of the brain [6]. These effects are becoming increasingly severe at higher field strength. Consequently, it is not surprising that an increasing number of papers have appeared in the recent past presenting different approaches to solve these problems.

The aim of this thesis is to give an overview of the fMRI data analysis focusing on some aspects of the preprocessing pipeline.

In the first chapter, we will introduce the problem of Echo Planar Imaging (EPI) spatial distortions and a new method to correct them. This method is based on the acquisition of a T2-Weighted (T2W) 3D volume to perform a non-linear registration of the EPI to the anatomical reference. We will compare the proposed method with other possible solutions using an acquired task-fMRI dataset.

The second chapter will show the procedure for the construction of a good reference to apply the EPI-distortions correction method. This is done through a new super-resolution algorithm to reconstruct an high resolution isotropic T2W reference starting from clinical images.

In the third chapter the proposed super resolution will be used to reconstruct a T2W reference which can be used to perform the EPI distortion correction method. We will show through a set of experiments how the resulted T2W volume can be used as good as the acquired T2W acquired scan.

Finally in the fourth chapter we will present a bunch of clinical fMRI studies where the correction method was performed. These studies involve different situations (group/single subject analysis and task/resting state fMRI) where our method was successfully used.

# Chapter 1 – EPI induced distortions correction

## 1. Introduction

The principles of Echo Planar Imaging (EPI) were first introduced by Sir Peter Mansfield in 1977 [15], however the very first snapshots of this sequence were introduced lately in the 1981 [16]. EPI is capable of significantly shortening MRI times, allowing acquisitions of images in the range of 20-100 msec [17]. These short times allow to evaluate fast changing physiological processes. This sequence is applied in multiple fields, which require fast acquisitions. The most prevalent clinical application of EPI is imaging of the brain. In perfusion imaging it's used to evaluate cerebral ischemia and differentiate recurrent tumors from radiation necrosis. In diffusion imaging, the EPI sequence is sensitized to the diffusion of water molecules. In functional imaging, the EPI sequence is used to evaluate the BOLD effect.

To understand the EPI sequence, we can compare it with conventional Spin-Echo (SE) imaging. In a SE pulse sequence, one line of imaging data (one line in k-space or one phase-encoding step) is collected within each Repetition Time (TR) period. The pulse sequence is then repeated for multiple TR periods until all phase-encoding steps are collected and k-space is filled. Therefore, the total acquisition time is equal to the product between the TR and the number of phase-encoding steps. However, if multiple Radio Frequency (RF) excitations are used for data averaging the imaging time increases. In EPI, multiple lines of imaging data are acquired after a single RF excitation. Like a conventional SE sequence, an EPI sequence begins with 90° and 180° RF pulses. However, after the 180° RF pulse, we have a rapid oscillation of the frequency-encoding gradient from a positive to negative amplitude: these oscillations form a train of gradient echoes. Each echo is phase encoded differently by phase-encoding blips on the phase-encoding axis. Each oscillation of the frequency-encoding gradient corresponds to one line of imaging data in k space, and each blip corresponds to a transition from one line to the next in k space (Figure 2). This technique is called blipped echo-planar imaging [18]. In the original echo-planar imaging method, the phase-encoding gradient was kept on weakly but continuously during the entire acquisition [19]. Today there are many variants on the sequence, for example in the asymmetric EPI data are collected only during the positive frequency-encoding gradient lobe, while the negative frequency-encoding gradient lobe is used to just traverse back to the other side of k space [20]. EPI can be performed by using single or multiple excitation pulses, also called “shots”. The number of shots represents the number of TR periods required to complete the image acquisition, and it is equal to the total number of phase-encoding steps divided by the echo train length. In single-shots EPI, all of the k-space data are acquired with only one shot. In multi-shots EPI, only a portion of the k-space data is acquired with each shot, and the shots are repeated until a full set of data is collected.

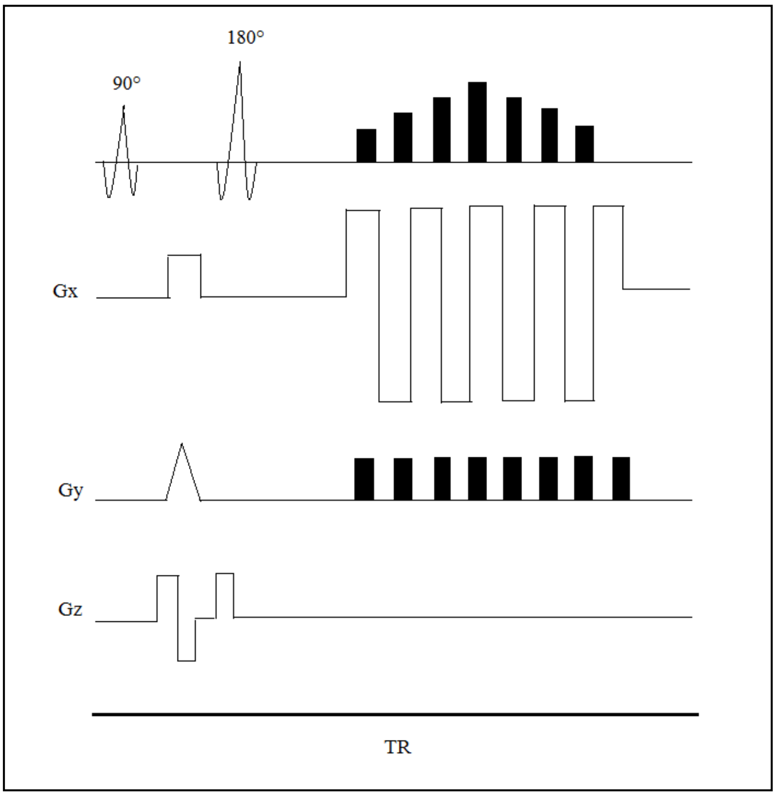

**Figure 2 - Echo-planar imaging sequence. Within each TR period, multiple lines of imaging data are collected. Gx = frequency-encoding gradient, Gy = phase-encoding gradient, Gz = section-selection gradient**

## 2. Advantages and disadvantages in EPI

EPI carries the advantage that the full magnetization is available for the image formation, without a penalty in overall imaging time. The imaging speed in EPI comes from the use of a very high amplitude field gradients with very rapid sampling. However EPI pays a penalty in bandwidth, which it refers to the difference in MR frequencies between adjacent pixels, as well to the total range of frequencies that make up an image. In conventional imaging, the bandwidth per pixel, is ordinarily kept comparable to the chemical shift between fat and water. The continuous encoding scheme used in EPI, instead, results in a relative low bandwidth along the phase-encoding axis (30 Hz/pixel is typical). This causes several difficult artifacts to occur in EPI.

**Chemical shifts artifacts** causes the displacement of fat and water of about 8 pixels in 1.5 T scanners, and this effect increases on higher field. Since mostly body tissues contain at least some water and fat, it is absolutely necessary to correct the problem. Luckly, there are a number of good techniques to manage chemical shift [21] Because only the water signal is of interest in fMRI, usually a 90° pulse at the fat frequency is applied prior to imaging, without significantly affecting water signal. After this pulse the fat signal will be in the transverse plane and it can be de-phased easily by applying a gradient pulse. Until the fat signal has had time enough to recover its longitudinal magnetization it will not appear in the images. An alternative approach is to use Short T1 Inversion Recovery (STIR) method [22]. This technique takes advantage of the T1 difference between fat and other body tissues. An 180° pulse is applied just before the EPI imaging sequence timed such that the magnetization of fat is recovering through zero at the time of the 90° excitation pulse. Because the fat has no magnetization at that time, the 90° pulse does not result in the formation of any signal from fat.

**Eddy currents** are another typical problem in EPI. These are currents inducted when the MR field gradients are switched on and off, generating a time varying magnetic field in the various conducting surfaces of the rest of the imaging instruments. These, in turn, set up magnetic field gradients that may persist after the primary gradients are switched off. Such eddy currents are a problem in both conventional imaging and EPI but are more severe in the latter because the gradient amplitudes, and particularly the gradient switching rates, used in EPI are much greater and induce larger eddy currents. Further, the long readout period in EPI results in more opportunity for image distortion artifacts. A particularly common EPI artifact is so-called "ghosting" from eddy currents. This results from the time-dependent frequency shift created by the time-dependent eddy currents. Because of the back and forth trajectory in k-space used in EPI, the frequency shifts create a phase difference from line to line in the raw data. When the data are Fourier transformed, the phase shift creates a phase ambiguity in the images, such that part of the signal appears 90° out of phase, or one half image away. The correction of image ghosts may take several forms. Probably the most robust scheme is to design the gradient coils critically such that eddy current induction is minimized, using shielded or screened gradient coils, in which a separate set of gradient coils is counter-wound around outside the primary coil set to cancel any external magnetic fields. Because gradient efficiency drops as the fifth power of the radius, even a small gap between primary and secondary gradients allows for a non-zero gradient inside the coil and a zero gradient outside [23]. An alternative approach to ghost correction is to acquire a reference scan in the absence of phase encoding and to use this as a basis for determination of the time-dependent phase shifts [24,25].

**Shape distortions** due to magnetization inhomogeneities are a much less manageable artifact. Even in a well-shimmed magnet, the human head will magnetize unevenly so that the MR frequency may differ from point to point by about 1 part per million (ppm). This causes spatial displacements of the signal in the resulting images, which are appreciable mainly in the phase encoding direction and may also change with motion of the subject in the scanner.

The phase evolution of a pixel in MRI is dictated by the local magnetic field that it experiences. In general for a point, the signal induced in the NMR receiver coil is given by

$$\partial S(x,y,z,t) \propto \rho(x,y,z) exp\left[i2\pi\gamma\int_0^t B_0(x,y,z)dt\right]\cdot exp\left[-t/T_2^{(*)}\right]$$

(1)

Where the time origin is the excitation pulse, $\gamma$ is the gyromagnetic ratio in Hz/Tesla, and $\rho(x, y, z)$ is the local spin density. In the case of a slice-selected imaging experiment, in which phase encode $G_p$ and read $G_r$ gradients are applied, and with field inhomogeneity term characterized by $\Delta B_0(x, y, z)$ the first exponential in Eq. (1) becomes

$$exp\left\{i2\pi\gamma\left[\left[\int_0^t G_r(t)xdt + \int_0^t G_p(t)ydt + \int_0^t \Delta B_0(x, y, z)dt\right]\right]\right\}$$

(2)

If we arbitrary define x to be the read direction and y to be the phase encode direction. In the k-space notation, the gradient history is characterized by making the substitution $k(t) = 2\pi\gamma \int G(t)dt$. In an EPI experiment, in which the whole of k-space is sampled following a single excitation of the sample, the phase evolution between adjacent points in k-space for the elemental pixel is given by

$$\Delta\Phi_r = 2\pi\gamma[G_r xDW + \Delta B_0(x, y, z)DW]$$

$$\Delta\Phi_{pe} = 2\pi\gamma\left[G_{pe} y\tau_{ramp} + \Delta B_0(x, y, z)(2\tau_{ramp}N.DW)\right]$$

(3)

Where $DW$ is the dwell time and $\tau_{ramp}$ is the ramp time of the switched gradients. We can see from Eq. (3) that both the read and phase encode pixel positions are affected by the field inhomogeneity term, but only the effects in the phase encoding direction are quite significant. Figure 3 shows an EPI slice acquired with different phase encoding directions.

The shape distortions are a frequent cause of concern in functional neuroimaging, as it is often desirable to superimpose regions of brain activation onto higher resolution structural images, which are usually acquired with a much higher bandwidth. In this case, functional EPI will not be registered properly with the structural dataset, resulting into an inaccurate spatial localization of brain activity, and also to errors in the statistical group analysis. Several possible retrospective solutions have been developed during the years. In the following part of this thesis we will discuss some of them.

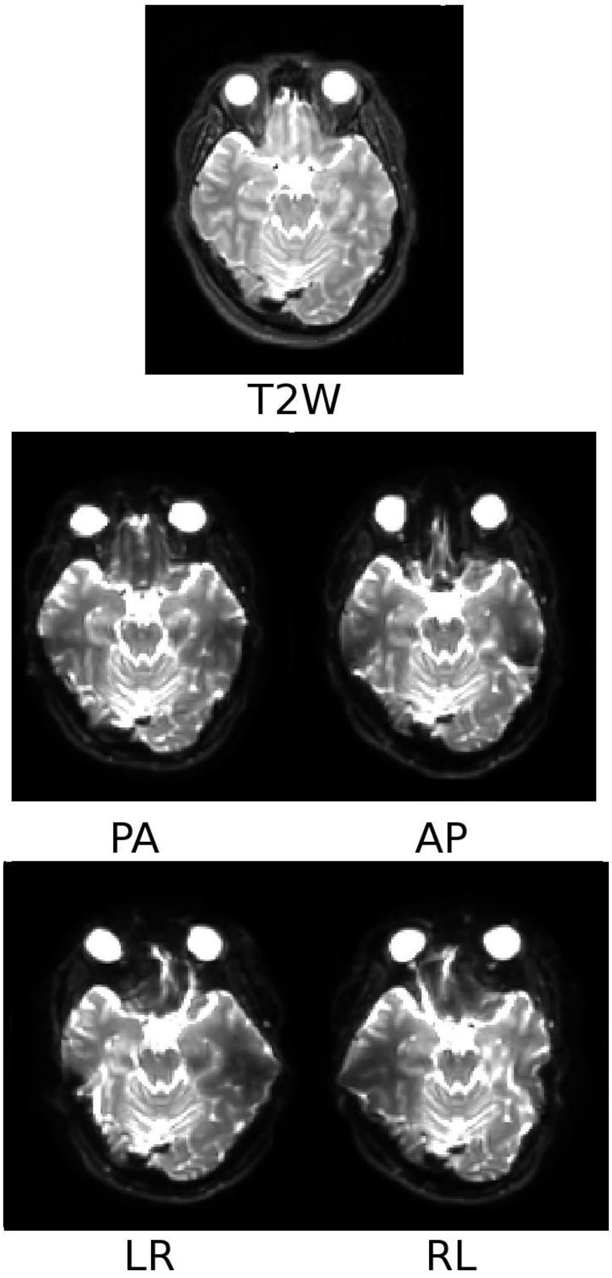

**Figure 3 - On top a T2W slice without geometric distortions. On the bottom the same slice, acquired with four EPI sequences with different phase encoding directions: Posterior-Anterior (PA), Anterior-Posterior (AP), Left-Right (LR), Right-Left (RL).**

# 3. Methods for Retrospective EPI-induced distortion correction

When we talk about retrospective algorithms for correcting shape distortions in EPI, we can recognize three main approaches: correction based on magnetic field mapping, correction making use of an additional EPI data with reversal of the phase-encoding direction, and correction performed with a non-linear registration to an undistorted anatomical reference. All of these methods relays on the acquisition of an additional sequence, which is used to perform the correction strategy. If no additional sequence is available, the distortion correction can't be performed. Figure 4 shows the flowchart preprocess analysis in fMRI, without any distortion correction strategy. As we can see, the raw-EPI data are corrected for subject motion with a rigid registration, then the average EPI is registered to the corresponding T1W which is normalized to the standard space.

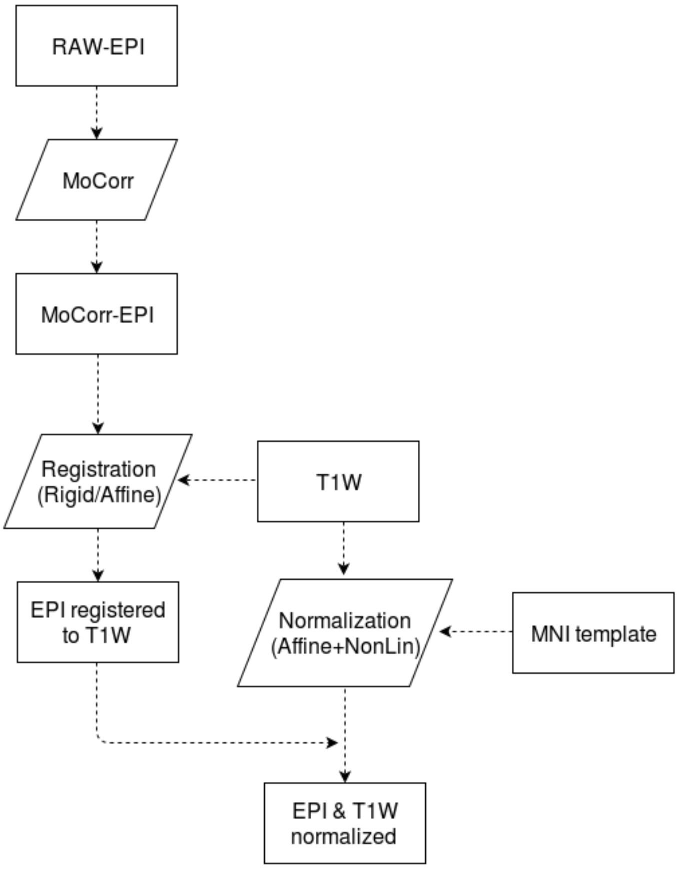

**Figure 4 - fMRI flowchart preprocess without any distortion correction strategy**

**Magnetic field mapping methods** relay on the acquisition of the spatial variation of the static field, measured by the phase difference of two gradient echo images acquired with different Time Echos (TE). This is used to unwarp the distorted EPI images [26]. Once the phase map from each of the gradients echo images has been calculated and the $\pi$ bounce points have been unwrapped, the field inhomogeneity map may be calculated according to $\Delta B_0(x,y,z) = (2\pi\gamma\Delta TE)^{-1}\Delta\Phi(x,y,z)$. An additionally step is to slightly smooth the images before calculating the phase map: this can help to have a smoother transition between inter-hemispheric gaps. Finally the field map is converted into a pixel shift map according to the equation:

$$\Delta r_{pe} = \gamma\Delta B_0(x,y,z).N\left(2\tau_{ramp} + N.DW\right)$$

(4)

Which is a simply a mathematical way of saying that the phase encode shift $\Delta r_{pe}$, in units of pixels, is equal to the measured field inhomogeneity $\Delta B_0(x,y,z)$, converted to Hz, and divided by effective spectral width per pixel $N\left(2\tau_{ramp} + N.DW\right)$. The location of a pixel in the geometrically distorted (warped) image is then related to the position of the pixel in the unwrapped image by the formula

$$y_{pe}^{w} = y_{pe}^{uw} + \Delta r_{pe}\left(y_{pe}^{uw}\right)$$

(5)

The main drawback of this method is the separate acquisition of the multi-echo images: subject movement between the field mapping and EPI acquisition could render the field map inaccurate. Furthermore, the phase unwrapping process is sensitive to noise. An alternative technique is to acquire a phase-encoded multi-reference scan to estimate the magnitude and phase errors due to field inhomogeneity, and then use that to correct the EPI artifact [27]. Figure 5 shows the flowchart diagram for the preprocess, including magnetic field mapping methods acting on the motion corrected EPI.

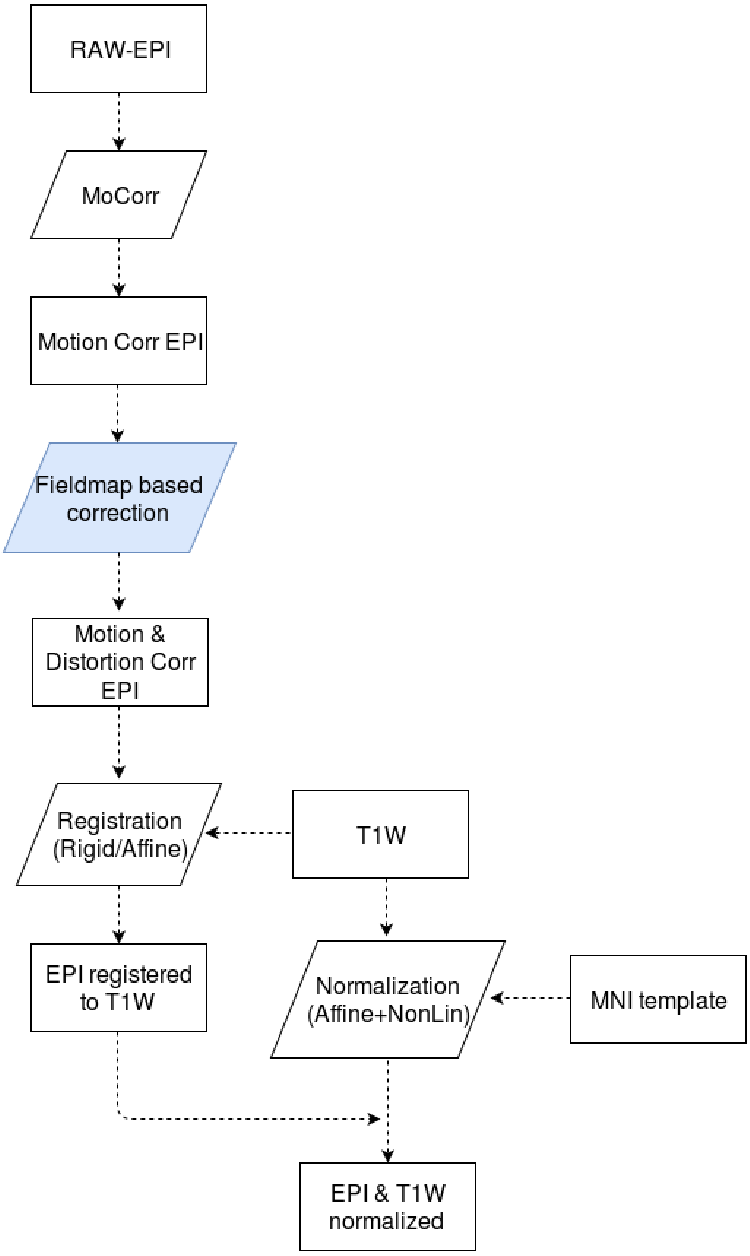

**Figure 5 - fMRI preprocess flowchart using the fieldmap based correction method. The correction is performed on motion corrected EPI (blue block)**

**Reversed phase-encoding corrections methods** relays on the fact that phase-encoding gradients with opposite polarities will produce opposite spatial and intensity distortions in the phase-encoding direction. Therefore an anatomically corrected image should be the one with minimal difference between the pair of distorted images [28,29,30]. The advantage of this method, compared to the field mapping method, is that the acquisition of an EPI with opposite polarity is on the scale of the seconds, while for the field map is on the scale of the minutes. This lead to these methods to be less sensitive to subject motion. However unwrapping on a single dimension may cause discontinuities in the other two dimensions. An improved version is to generate a continuous and smooth 3D displacement field [31]. In this implementation the two echo-planar images, once traversing k-space bottom-up and once top-down, have identical magnitude distortions in opposite directions. Using these acquisition with a model for the image formation process of spin-echo EPI, lead to estimate the underlying magnetic field map and undistorted images.

Let us denote the true space as $\mathbf{x} = [x, y, z]^T$, the space of a bottom-up acquired EPI image as $\mathbf{x}_+ = [x_+, y_+, z_+]^T$, and that of a top-down EPI by $\mathbf{x}_- = [x_-, y_-, z_-]^T$. Furthermore, let us denote the mapping $\mathbf{x} \rightarrow \mathbf{x}_+$ by $T_+$ and the mapping $\mathbf{x} \rightarrow \mathbf{x}_-$ by $T_-$. Both mappings are uniquely determined by a displacement field $d(\mathbf{x}) \propto \Delta B_0(\mathbf{x})$ where $\mathbf{x}_+ = T_+(\mathbf{x}) = [x, y + d(\mathbf{x}), z]^T$ and $\mathbf{x}_- = T_-(\mathbf{x}) = [x, y + d(\mathbf{x}), z]^T$. The process of finding the $\Delta B_0(\mathbf{x})$ field that results in two observed datasets of $f_+(\mathbf{x}_+)$ and $f_-(\mathbf{x}_-)$ can be thought of as finding the displacement field $d(\mathbf{x})$ that fulfills

$$\left|\frac{\partial(\mathbf{x}_+)}{\partial(\mathbf{x})}\right|_{x_+} f_+(\mathbf{x}_+) = \left|\frac{\partial(\mathbf{x}_-)}{\partial(\mathbf{x})}\right|_{x_-} f_-(\mathbf{x}_-)$$

(6)

For every $\mathbf{x}$.

$\Delta B_0(\mathbf{x})$ is modeled as a linear combination of basis warps consisting of a truncated 3D cosine transform. This will be noted as $\Delta B_0(\mathbf{x}, \mathbf{b})$ where $\mathbf{b}$ is the vector of weights of the basis warps. Similarly is the concept for $d(\mathbf{x}, \mathbf{b})$. The estimation model for $\mathbf{b}$ is

$$\boldsymbol{b}_i = \boldsymbol{b}_{i-1} + \left( \left[ \left(\frac{df_+}{d\boldsymbol{b}}\right)^T \left(\frac{df_-}{d\boldsymbol{b}}\right)^T \right] \begin{bmatrix} I & -I \\ -I & I \end{bmatrix} \begin{bmatrix} \frac{df_+}{d\boldsymbol{b}} \\ \frac{df_-}{d\boldsymbol{b}} \end{bmatrix} \right)^{-1} \times \left[ \left(\frac{df_+}{d\boldsymbol{b}}\right)^T \left(\frac{df_-}{d\boldsymbol{b}}\right)^T \right] \begin{bmatrix} I & -I \\ -I & I \end{bmatrix} \begin{bmatrix} f_+ \\ f_- \end{bmatrix}$$

(7)

For i=1,2,….. where it is assumed that any difference between $f_+$ and $f_-$ can be attributed to susceptibility effects. The model also can include a rigid-body movement to take in account subject motion.

Figure 6 show the flowchart diagram for the fMRI preprocess, including reversed phase-encoding correction methods acting during the motion correction step.

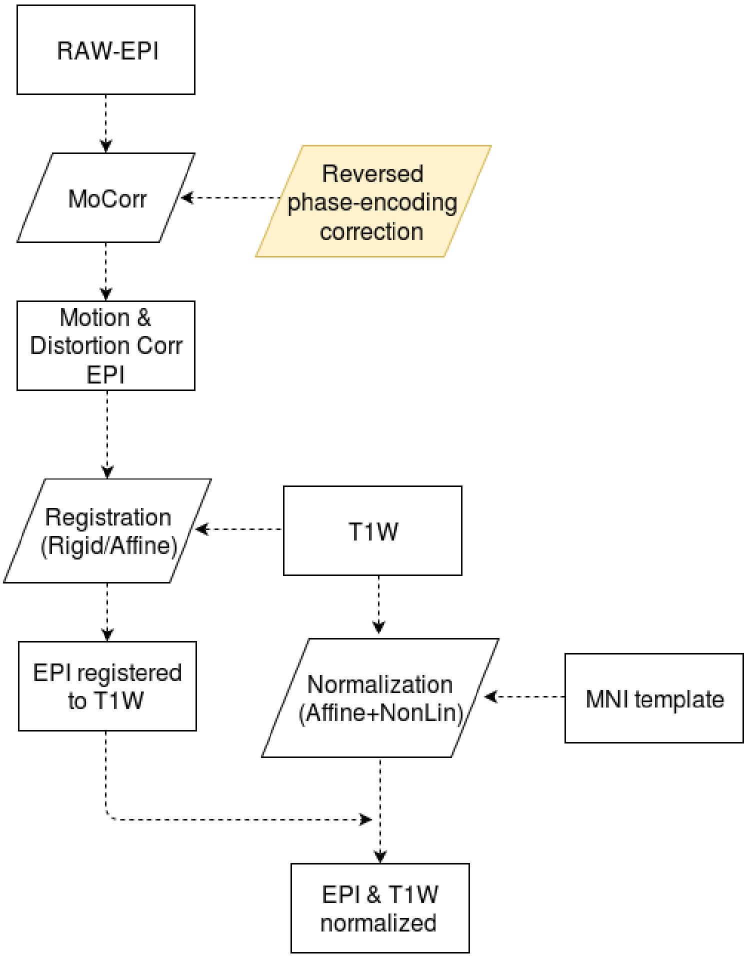

**Figure 6 - fMRI preprocess flowchart using the reversed phase-encoding correction strategy. The method is applied during the motion correction step (yellow block)**

**Non-linear registration methods** to an anatomical correct image can also be performed to adjust for susceptibility artifacts. In [32] they developed a multi-resolution approach to align EPI to the corresponding anatomical reference, modeling the deformation field with splines and using the least-squares criterion for the registration. Considering $g$ as a bivariate warping function, it can be described by

$$g(\boldsymbol{x}) = \sum_{k \epsilon K} c_k \beta_3(\boldsymbol{x}/h - k)$$

(8)

Where $c_k$ are a set of parameters of the model, $h$ is the knot spacing and $K$ is the set of indexes of the spline functions.

In [33] a non-rigid registration of a spin-echo EPI is performed on a T1W sequence, using constraints regarding the smoothness of the solution. They make use of an entropy-based registration criterion to evaluate the mapping of T2W EPI onto the anatomical T1W image, using the log-intensity of the criterion to provide increased sensitivity in areas of low EPI signal. The key step on which this paper is based is to make direct use of constraints derived from the underlying MR imaging model within a non-rigid registration algorithm. The distortion field between anatomical MRI and spin echo EPI is parameterized by a regular B-spline. In Figure 7 we can see the flowchart diagram for fMRI preprocess, including the registration based correction strategy.

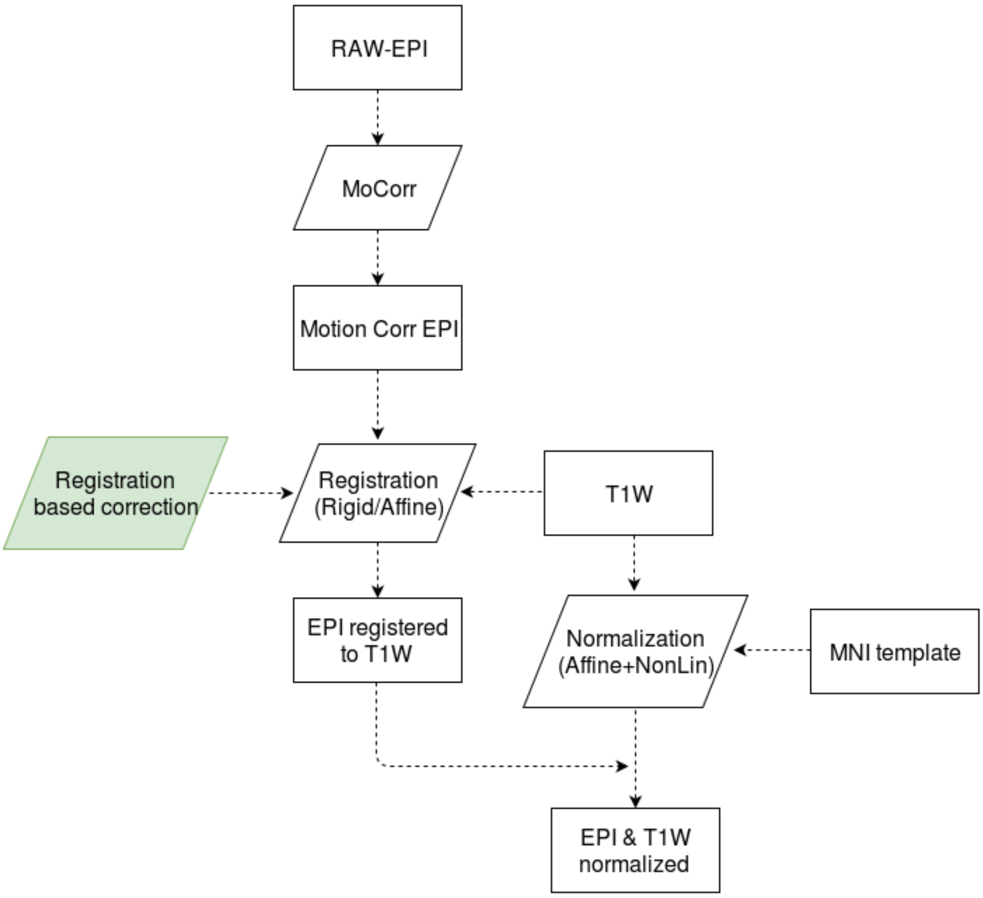

**Figure 7 - fMRI preprocess flowchart using the registration based correction strategy. The method is applied during the registration of EPI to an anatomical reference (green block)**

## 4. Proposed method for EPI-distortion correction

As we could see in the previous part of this chapter, each one of the method to correct for EPI geometric distortions relays on the acquisition of another sequence: the B0 inhomogeneity for the magnetic field mapping methods, an EPI with opposite polarity in the phase-encoding direction for the reversed phase-encoding correction methods, and an anatomical sequence for the non-linear registration methods. Some of these sequences are acquired with the only purpose of distortion correction (e.g. field map, reversed phase-encoding direction), while they have no use for any clinical application. Moreover, in some cases functional datasets may have been already acquired without any planning for the presence of distortions, i.e. without acquiring the field map or the reverse phase encoding images. In this case, we should think of a way to perform some sort of correction with the only available data.

In the following part we will describe our new proposed method to correct for EPI geometric distortion. T1W sequences are normally acquired during a standard fMRI exam to map brain activations onto an high resolution anatomical reference. The assumption is that, in absence of distortions, EPI and T1W images of the same subject share the same anatomical structure, and a rigid registration with just 6 Degrees of Freedom (DoF) is quite appropriate to match them. However, in presence of distortions, this assumption is no longer valid, and a higher DoF transformation is required to reach the optimal match. Due to the different tissue contrast between EPI and T1W acquisitions, deformable registrations (i.e. with more than 12 DoF) are not recommended to directly map the EPI data onto the T1W one. Our method takes advantages of a T2W isotropic volume to perform a non-linear registration (and the distortion correction) as an intermediate step before matching the EPI to the T1W volume. The alignment between EPI and T2W is performed in a two-step registration: firstly an affine (12 DoF) transformation is performed to reach a raw match of anatomical structures, then a Symmetric diffeomorphic Normalization (SyN) model [34,35] is applied to perform the non-linear part of the registration. This method guarantees sub-pixel accurate and invertible transformations in the discrete domain by directly including invertibily constraints in the optimization. Let's define a diffeomorphism $\varphi$ of the domain $\Omega$ which transform the image $I$ into a new coordinate system by $\varphi I = I \circ \varphi(\boldsymbol{x}, t = 1)$, where $t$ is the time, $\boldsymbol{x}$ is the spatial coordinate and $\varphi(\boldsymbol{x}, t = 1)$ is the velocity field (also defined as $v(\boldsymbol{x}, t)$). $\varphi$ is gained by integrating the velocity fields in time, $\varphi(\boldsymbol{x}, 1) = \varphi(\boldsymbol{x}, 0) + \int_0^1 v(\varphi(\boldsymbol{x}, t), t) dt$; the distance is then $D\big(\varphi(\boldsymbol{x}, 0), \varphi(\boldsymbol{x}, 1)\big) = \int_0^1 \|v(\boldsymbol{x}, t)\|_L dt$, where $L$ defines the linear operator regularizing the velocity. The functional norm $\|\cdot\|_L$ induces regularity on the velocity field via a linear differential operator such as $L = a\nabla^2 + b\boldsymbol{Id}$ ($a$, $b$ contants). The image registration diffeomorphism can be divided in two parts $\varphi_1$and $\varphi_2$and with this the two image $I$ and $J$, that have to be registered, contribute equally to the path and the deformation is divided between them. The resulting formulation is $D\big(\boldsymbol{Id}, \varphi_1(\boldsymbol{x}, 0.5)\big) = D\big(\boldsymbol{Id}, \varphi_2(\boldsymbol{z}, 0.5)\big)$ where $\boldsymbol{x}$ is the identity position of some anatomy of the image $I$ and $\boldsymbol{z}$ is the identity position of the same anatomy in the image $J$.

The SyN solution is to find $\varphi_1$ and $\varphi_2$ which minimize the following functional

$$E_{sym}(I,J) = \int_0^{0.5} \{\|v_1(x,t)\|_L^2 + \|v_2(x,t)\|_L^2\}dt + \int_\Omega \left|I\big(\varphi_1(0.5)\big) - J\big(\varphi_2(0.5)\big)\right|^2 d\Omega$$

(9)

For our application, we used the cross-correlation similarity metric implementation of the SyN model. Cross-correlation measure was chosen because allows robust matching of images, due to the locally adaptive character, better than the mutual information measure. Also, as we could see in the previous chapter, most of the EPI geometric distortions are characterized in the phase encoding orientation; for this reason we constrained the deformation field to act mostly in this direction.

Our complete preprocess pipeline, including the registration explained above, can be summarized in Figure 4. The raw EPI are firstly realigned with a rigid registration (slice time correction, to compensate for differences in acquisition times, can be considered an optional step), then the average EPI is registered to the T2W volume with the method explained above to obtain the transformations that will be applied to the whole 4D functional realigned sequence. The T2W is rigidly registered to the T1W volume and, while T1W is normalized to the standard MNI space with an affine and a non-linear registration for group analysis purpose. Smoothing of functional data is finally performed to increase the SNR before computing the GLM.

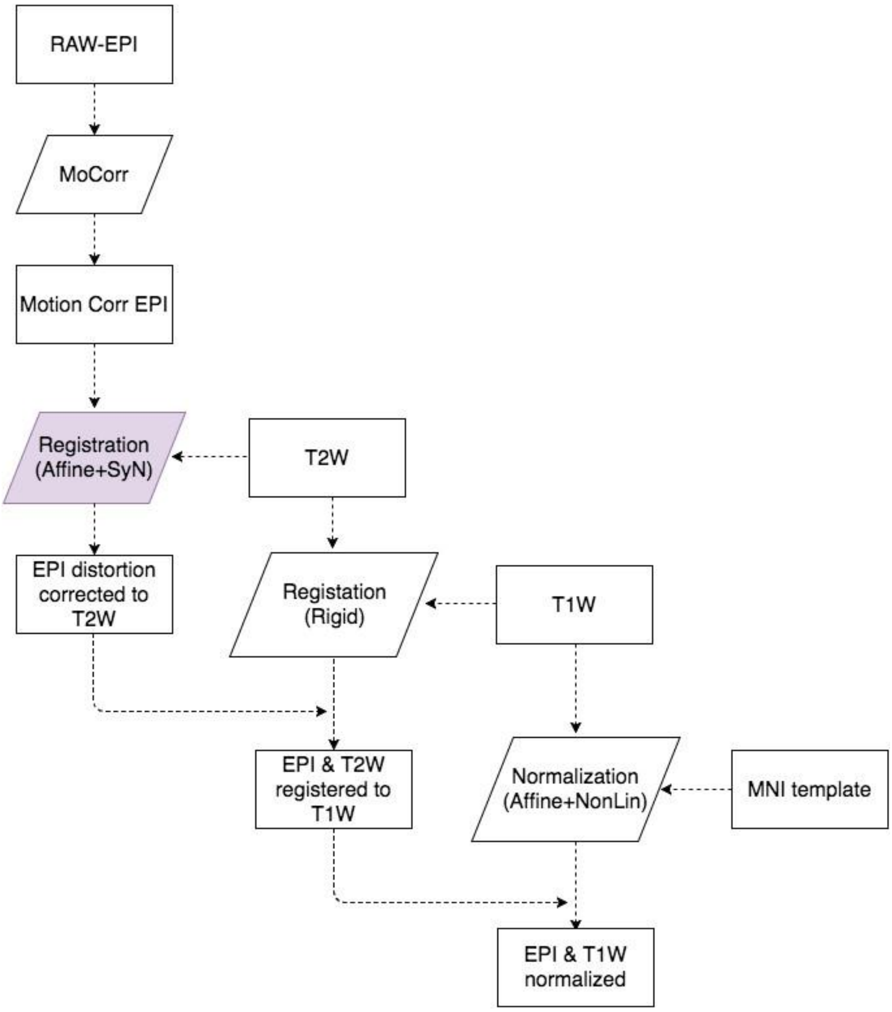

**Figure 8 – fMRI preprocess flowchart using the proposed strategy. Motion corrected EPI are registered to the T2W reference using a two step registration (affine and SyN restricted mainly to the phase encoding direction), Then T2W is rigidly registered to the TW1 which is normalized to the standard space.**

## 5. Material and experiments

To evaluate the performances of our method we acquired an fMRI dataset of a block design visual task. The task was the grating stimulus task [36] consisting of 18 sec blocks of M-stimuli, P-stimuli and baseline (fixation point). M and P stimuli were both full-field sinusoidal gratings with sinusoidal counter-phase flicker. The gratings were presented at one of 6 orientations (0°, 30°, 60°, 90°, 120° and 150°) and changed to a new random orientation every 3 sec. The M-stimulus was a 100% luminance contrast, black-white grating with a spatial frequency of 0.5 cpd and a flicker frequency of 15 Hz. The P-stimulus was a low luminance contrast, high color contrast red-green grating with a spatial frequency of 2 cpd and a flicker frequency of 5 Hz. To guarantee the subject attention during the exam, a target detection task was implemented during the M and P stimuli blocks: targets were 2D Gaussian contrast decrements presented for 300 msec. After each M or P stimulus block, we asked to subjects to press a button on a MRI compatible pad if they saw the target stimulus during the block.

We recruited fifteen young healthy subjects (mean age = 14.0 ,std = 1.6 , 12 males). The acquisition protocol included a T1W sequence (TR = 8 msec, TE = 3.5 msec, filp angle 8°, voxel size 1 $mm^3$ isotropic, matrix size 256 x 256 x 160) a T2W fat suppressed scan (TR = 4700 msec, TE = 100 msec, voxel size 1.5 $mm^3$ isotropic, matrix size 160 x 146 x 110) an fMRI sequence (TR = 2 sec, TE = 40 msec, voxel size 3 $mm^3$ isotropic, matrix size 80 x 80 x 39, flip angle 90°, 348 time points), a field map acquisition (TR = 650 msec, TE = 7 msec, flip angle 80°, voxel size 2.6 $mm^3$ isotropic, FOV 250 x 250 $mm^2$) and a set of 10 blip-up and blip-down EPI volumes (same parameters as the fMRI sequence, except for the inverted phase-encoding direction). One subject was discarded from the analysis due to an heavily corrupted T1W sequence.

Our purpose is to demonstrate that the correction of EPI distortions impacts significantly on the group level analysis, and that our method has good performances in doing that. We than compared the proposed approach with a couple of other well known correction methods: one belonging to the field mapping acquisition strategy (FUGUE, FSL [26]), and one from the reversed polarity strategy (TOPUP, FSL [31,37]).

Briefly, we tested for four different analysis pipelines:

1. Without any correction for EPI distortions
2. The proposed correction method
3. The correction with FUGUE
4. TOPUP.

The only difference between these approaches was the distortion correction strategy, while any other preprocess step was performed exactly in the same way. T1W bias field inhomogeneity were corrected with the algorithm N4 implemented in Advanced

Normalization Tools (ANTs) [38,39]. T1W and T2W volumes were skull stripped with BET [40] implemented in FSL. Functional volumes were realigned using a rigid transformation, to the first volume of the sequence and then to the average EPI; alignment of the EPI to the corresponding anatomical T1W reference was performed through the T2W step for our method, instead for all other approaches it was directly reached with an affine transformation. All registrations were performed with ANTs except for the realignment step that was performed with the tool MCFLIRT [41] implemented in FSL. The single subject GLM analysis, and the t-test for group level analysis were performed with SPM12 [42]. The transformations to reach the standard MNI space were generated through the T1W study group template construction implemented in ANTs [44]. We then performed the segmentation of the T1W template using FAST [45] implemented in FSL. Single subject analysis was performed in the functional native space, after applying a 3D Gaussian spatial filter with Full Width at Half Maximum (FWHM) equal to 6 mm. Contrast maps were then projected to the standard space using the appropriate transformations for each strategy under exam. . In each case, the appropriate transformations were combined to perform a single interpolation operation, thus minimizing the interpolation errors. The final resolution was the same of the native space (3 mm isotropic). Then we furtherer smooth the contrast images in the template space with different smoothing levels to evaluate its impact on the results. In particular, we selected three different levels: no further smoothing, a Gaussian filter with 3 mm of FWHM (mid smoothing level), and another one with 6 mm of FWHM (high smoothing level).

The first experiment was meant to evaluate the performance of the different pipeline analysis with respect to the smoothing level. We computed the average group activation performing a one-group t-test for each one of the four approaches, evaluating the average group activation. Lacking of a ground truth, we used physiological criteria to determinate the goodness of the activation: significant activations in White Matter (WM) and Cerebro-Spinal Fluid (CSF) were labeled as false positive, while only Gray Matter (GM) activations were considered true. Using the GM mask in the template space, we computed the percentage of GM active voxels with respect to the total amount of active voxels, considering different smoothing levels and t-values for the significance threshold.

In the second experiment we wanted to compare directly the different correction strategies with a paired t-test. Pairs were defined using contrast images belonging to the same subjects with different analysis approach. This lead us to evaluate which regions resulted with higher significance with one method respect to the other. For this purpose, we generated a mask merging the activations obtained with the four approaches: this was used as an implicit mask for the paired t-test (to consider only anatomical regions truly involved in the task). To significantly improve SNR and the homogeneity of the maps, only contrasts with the highest smoothing level (6 mm) were tested.

## 6. Results

Figure 9 shows the average group activation for the proposed approach for the comparison M-stimulus versus baseline, using a $p<0.05$ corrected for the False Discovery Rate (FDR) and a minimum cluster size of 10 voxels (270 $mm^3$). As expected from a visual task, it involves occipital cortex brain regions, corresponding to the primary and the extra-striate visual cortex. We can also see that the task involves brain structures corresponding to the Magno-cellular dorsal pathway on the parietal lobe.

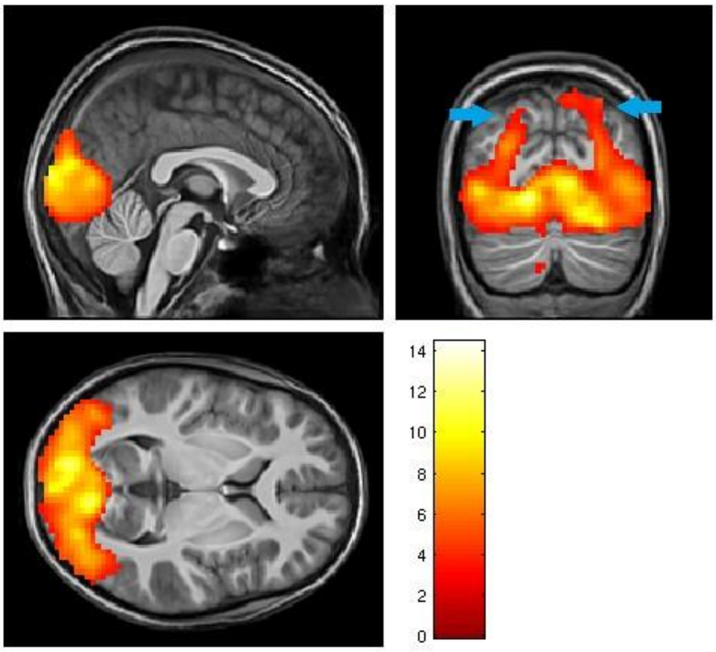

**Figure 9 - Average activation (proposed method) of the group for the contrast M-stimulus > Baseline. Significance was set using p<0.05 with FDR correction. Blue arrows show the dorsal stream of the Magno-cellular pathway.**

Figure 10 shows the results from the first experiment. The three plots represent three different level of smoothing, while different lines in each plot correspond to a different pipeline. Considering t-values thresholds between a p<0.001 uncorrected and a p<0.05 with Bonferroni correction (labeled with black stripped lines), the proposed approach has always higher percentage of GM active voxels than the other methods.

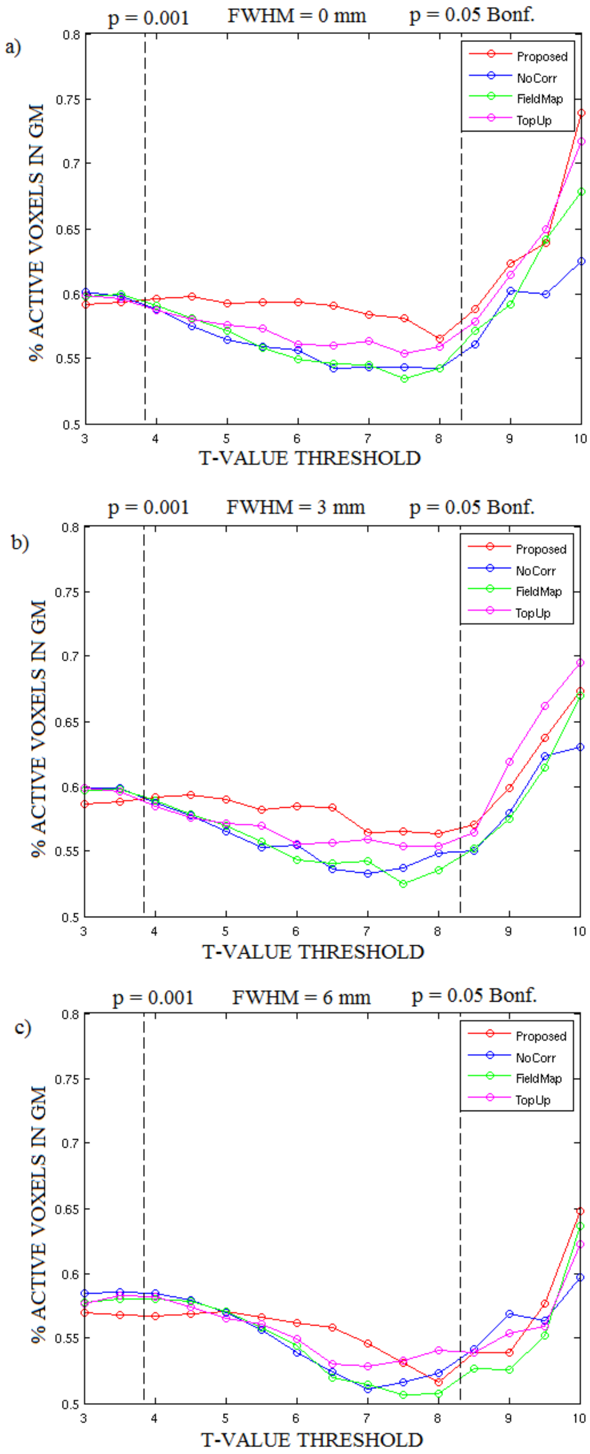

**Figure 10 - Percentage of active voxels in GM for the group level analysis with 3 smoothing levels, for different t-value thresholds. Smoothing levels go from no further smoothing after GLM (a), a Gaussian smoothing with FWHM equals to 3mm (b), and equals to 6mm (c). Black dashed lines label t-values corresponding to $p < 0.001$ uncorrected, and a $p < 0.05$ with Bonferroni correction thresholds**

We can see also that increasing the smoothing level decreases the overall percentage of GM activation, and also the differences between pipelines. Figures from 11 to 15 show the results from the paired t-tests. In Figure 11 the result from the comparison between the proposed method and the pipeline without correction. In Figure 12 the comparison between the proposed method and the pipeline with FOGUE. In Figure 13 the comparison between the proposed method and the pipeline with TOPUP. In Figure 14 the comparison between the pipeline with FOGUE and the one with TOPUP. In Figure 15 the comparison between the pipeline with TOPUP and the one without correction. No significant difference emerged from the comparison between the field mapping method approach and the uncorrected pipeline. As we can see the proposed approach has always higher significant voxels located on occipital cortex regions and parietal cortex regions respect to all the other strategies. Compared to the our method, both FUGUE and TOPUP strategies have higher significant voxels located mostly on white matter or in the proximity of tissue interfaces. Finally, from our results, field mapping correction strategy has no significant difference on the group level analysis compared to the approach without correction.

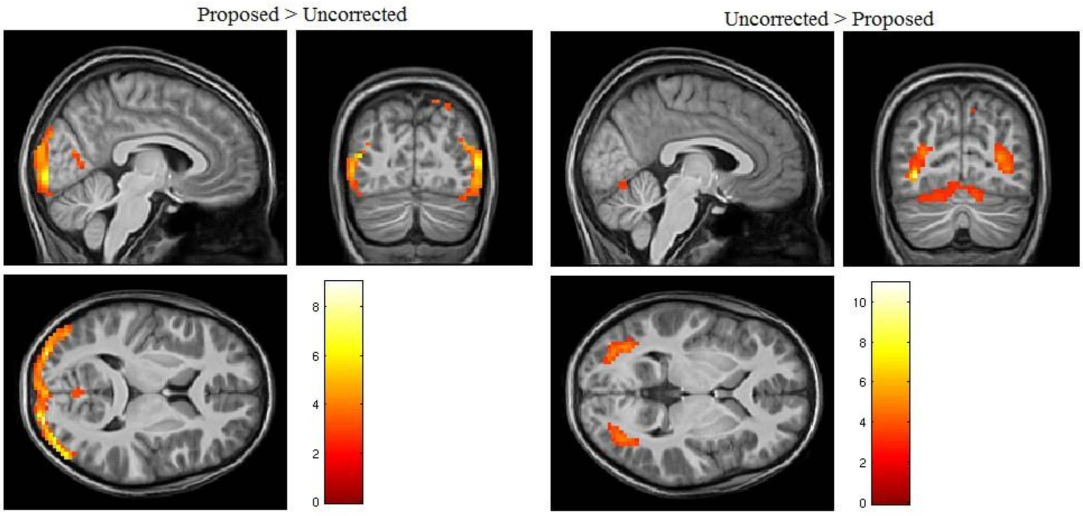

**Figure 11 - Paired t-test between the proposed method and the pipeline without correction. Left: higher significance for proposed method. Right: higher significance for the pipeline without correction. Significance was set to p<0.05 FDR corrected**

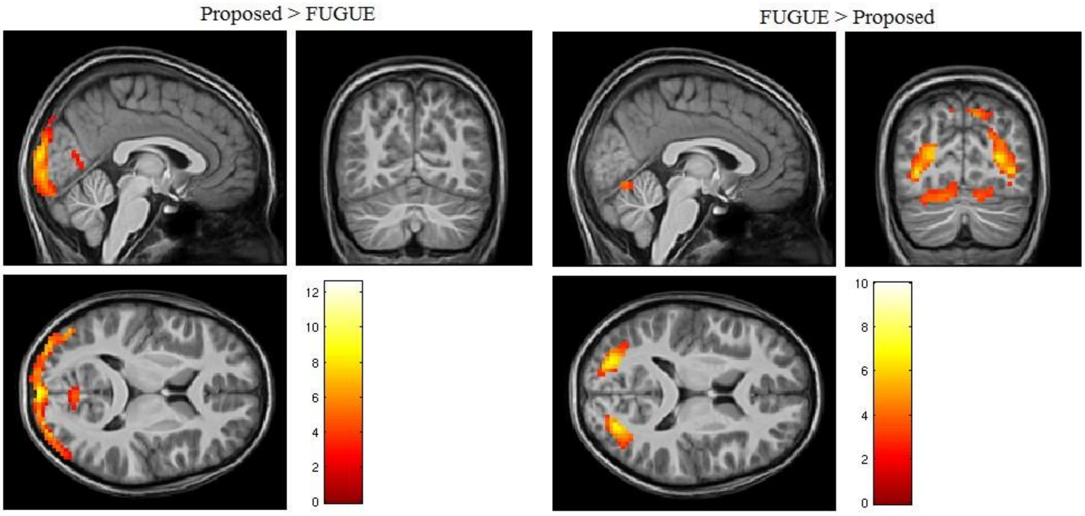

**Figure 12 - Paired t-test between the proposed method and the field mapping correction (FUGUE). Left: higher significance for proposed method. Right: higher significance for the field mapping correction approach. Significance was set to p<0.05 FDR corrected**

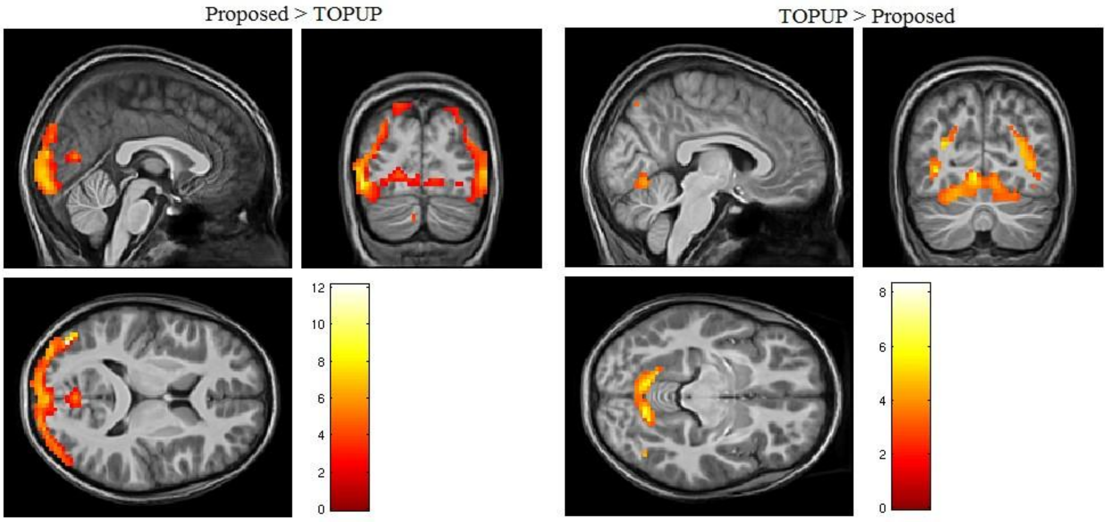

**Figure 13 - Paired t-test between the proposed method and the pipeline with TOPUP. Left: higher significance for proposed method. Right: higher significance for pipeline with TOPUP. Significance was set to p<0.05 FDR corrected**

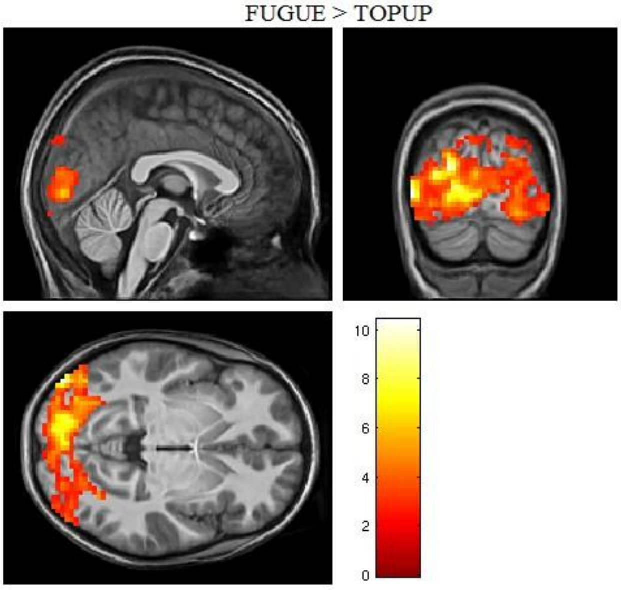
FUGUE > TOPUP

**Figure 14 - Paired t-test between the field mapping correction approach and the pipeline with TOPUP. Only the field mapping approach has higher significant voxels. No higher significance for the TOPUP pipeline. Significance was set to p<0.05 FDR corrected**

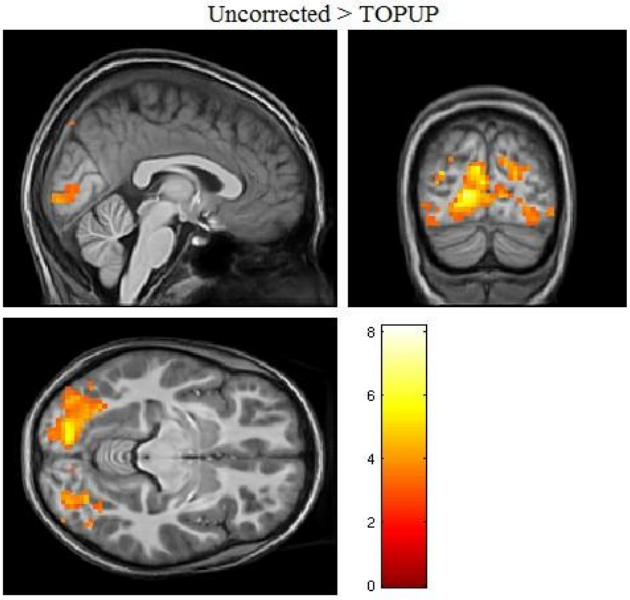
Uncorrected > TOPUP

**Figure 15 - Paired t-test between the pipeline with TOPUP and the pipeline without correction. Only the approach without correction has higher significant voxels. No higher significance for the TOPUP pipeline. Significance was set to p<0.05 FDR corrected**

# 7. Discussion

In chapter 1 we introduced the basis of EPI acquisition with a focus on the fMRI application. We explored the EPI sequence, and the different artifacts that affect the resulted images. Some of these artifacts can be reduced during the exam using proper acquisition parameters and correction strategy, and they don't need any post-processing techniques. However EPI-induced geometric distortions due to the inhomogeneity of the static magnetic field can be really problematic and need to be corrected to map brain activity onto the right anatomical structures. We briefly explored the state of art of the distortion correction techniques, and how they are applied to reduce this unwanted effect on EPI images. Finally, we proposed a new correction approach based on the acquisition of a T2W isotropic volume, which can be used as a reference to perform not only an affine, but also a deformable constrained registration. Using this intermediate step between the EPI motion correction intra-sequence and the registration to the T1W reference, we can improve the match between EPI and the anatomical reference. The validation of EPI distortion correction methods is an hard task, due to the difficulty to find a ground truth. Real datasets or phantom (not brain-EPI) datasets are usually employed to verify the effectiveness of the method. To validate the proposed method we made use of a real task-fMRI dataset. This dataset was pre-processed using different approaches, involving state of art correction methods, and the one without performing any distortion correction technique. Our experiments show that distortion correction techniques impact significantly on the group level analysis: in the paired t-test experiment significant differences were seen for almost all the comparisons (an exception was the comparison between field map correction methods and the approach without correction). A physiological criteria was chosen to evaluate the goodness of activation clusters: we should expect the BOLD effect in GM, while WM and CSF active voxels were labeled as false positive outcomes. The proposed method showed higher activation in GM occipital cortex compered to all the other approaches, and an higher significance for the dorsal stream compared to the approach without correction and TOPUP. These results suggest that the correction using a T2W as intermediate step provides a good registration of the subjects in the standard MNI space, increasing the significance for the t-test. Also different percentage of active voxels in GM were seen in the first experiment. A general higher percentage of GM active voxel for the proposed approach is an index of the good performances of our approach, compared to the other pipelines. Our group was firstly composed by fifteen subjects, however as we said in the previous paragraph, one subject was discarded due a corrupted T1W sequence, which produced registration errors between the EPI and the T1W. This wasn’t the case for the proposed pipeline, which performed quite good even in this situation. Considering that a lot of studies involve small group (e.g. in rare diseases studies), losing even just few subjects is not a trivial problem.

To conclude, our experiments have some intrinsic limitations: our results can’t be generalized (e.g. different scanners, field strength, and so on) but they are limited to this case study. Also the lack of a ground truth forced us to choose an alternative physiological criteria. Better and more general results can be obtained through simulated experiments, or using different EPI acquisitions and protocols.

# Chapter 2 - Super-Resolution 3D reconstruction of T2-Weighted images

## 1. Introduction

In MRI, different types of acquisition protocols are commonly used to acquire images with a different kind of contrast and resolution. Morphological acquisitions, such as T1W and T2W, are usually exploited in diagnostic tasks to evaluate malformations and lesions. However, only T1W are routinely acquired with an isotropic resolution and with a 3D acquisition protocol. On the other hand, acquiring T2W sequences with a high isotropic resolution is not feasible due to acquisition constraints such as the limited acquisition time, the low SNR and the subject motion during the scan. The acquisition of the 3D T2W image with a good isotropic spatial resolution (e.g. ~1 mm$^3$) with a good SNR takes longer than a T1W image, thus it is more sensible to motion artifacts. In the clinical practice, when a 3D sequence is not effective or possible, multiple sets of 2D slices are usually acquired. Moreover, 2D images can be acquired with a very high in-plane resolution (e.g. up to 0.2x0.2 mm$^2$), but also a very high slice thickness (even 8-9 times larger than the in-plane voxel size) in order to keep a good SNR. A common strategy is the acquisition of multiple 2D stacks with different orientations to give a better understanding of the normal anatomy and/or lesions. However, the high level of partial volume effect makes this approach not suitable for accurate quantitative measures, such as the volume quantification of specific structures. Therefore, the use of these images remains in the field of qualitative evaluations, usually performed by the radiologists. Quantitative measurements, such as cortical thickness or white and gray matter volumes, are often computed on T1-weighted (T1W) sequences due to the good tissue contrast. However, typical scanners reach a maximum resolution of 1 mm isovoxel. A possible solution to this problem is to apply post-acquisition image process techniques to increase the spatial resolution, highlighting the information content and increasing the diagnosis possibilities [46]. These techniques are based on the Super-Resolution Reconstruction (SRR) concept, commonly defined as the idea of creating a high-resolution image from several low-resolution images of the same subject. The main advantage of this approach is that it creates a high-resolution 3D volume with isotropic voxels, which can be used for many purposes such as volume quantification, diagnosis , and as element for further analyses (e.g. as a reference for perform EPI distortion correction).

The principle of the super-resolution algorithms is to combine several low-resolution images acquired in slightly different spatial orientations to estimate the single high-resolution source image that best explain them [47].

In this chapter we will resume the state of art of super-resolution algorithms in MRI, and then we'll propose a new pipeline to reconstruct an isotropic high-resolution 3D volume of the brain using three orthogonal T2W sequences (along the axial, coronal and sagittal directions) and a T1W 3D sequence of the same subject.

## 2. Super-Resolution Methods

One of the main advantages of SRR techniques is to retrieve additional information content from the combination of multiple low-resolution images into a higher-resolution one. The MRI framework is particularly well adapted to the application of these algorithms because of the control one has over the acquisition process [47]. Previous works demonstrated the benefits of using SRR methods over the direct acquisition at high-resolution images [48,49]: the main one is the reduction of the acquisition time. The acquisition of a high-resolution isotropic T2W image can be prohibitive in the clinical setting because of the too long acquisition time or the small SNR. Therefore, in the standard clinical and research practice, multiple 2D T2-weighted images are usually acquired in place of a single 3D volume. When multiple T2-weighted sequences are acquired, two different approaches can be applied: we can acquire stacks of parallel slices, or multiple slice slices with different orientations. First experiments in the SRR field were based on the former approach. For example, in [47] the authors acquired three multi-slice FSE at a resolution of 1 x 1 x 3 mm$^3$, each one shifted of 1 mm along the slice selection direction, and reconstructed a 1 mm$^3$ isotropic volume using an iterative algorithm. However, the second acquisition approach leads to a more efficient sampling of the k-space, and minimizes the redundancy between acquired volumes [50].

Different approaches can be followed with respect on which domain we are working on:

frequency, wavelet or image domain. In this thesis we will focus only on SRR in image domain, since recent studies [51] shown that they give the most accurate results. These methods are based on the inversion of the acquisition model that, without loss of generality about the dimension of the problem, can be expressed by the following equation:

$$Y_k = W_k X + V_k,\;\; k = \{1, \dots, N\} \tag{10}$$

where $Y_k$ represents the kth low resolution image, $X$ is the high resolution source image, $V_k$ is the acquisition noise in the kth image (often assumed to be a zero mean Gaussian process) and $W_k$ represents the global transformation operator that degrade the high resolution image to obtain the kth lower resolution one (with $N$ the total number of low resolution images). The latter takes into account the geometric transformation $G_k$, the blur introduced by the Point Spread Function (PSF) of the imaging model $B_k$ and the down-sampling operator $D_k$. Thus, $W_k$ can be rewritten as $W_k = D_k B_k G_k$. Computing the inversion of $W_k$ is an ill-posed problem, so optimization methods are usually employed to find the best solution. Several approaches have been proposed in literature, such as the Iterative Back-Projection (IBP) [52,53], the Deterministic Regularized Approach [54,55,56], the Statistical Regularized Approach [57,58] and Example-Based Methods [59,60].

The **IBP methods** [52,53] solves the problem estimating an high resolution volume from a set of low resolution images using eq. 10 and minimizing the difference between the simulated and acquired low resolution images. This is done through an iterative approach where the current estimation of the high resolution image is updated by the following procedure:

$$\hat{X}^{(n+1)}(x) = \hat{X}^{(n)}(x) + \ldots\ldots + \sum_{y \in \cup_k \Delta_{k,x}} \left( Y_k(y) - \hat{Y}_k^{(n)}(y) \right) \times h_{xy}^{BP} \tag{11}$$

where $\hat{\mathrm{X}}^{(\mathrm{n})}$ is the estimation of the high resolution image at the nth iteration, $\mathrm{Y}_\mathrm{k}$ is the kth acquired low resolution image, $\hat{\mathrm{Y}}_\mathrm{k}^{(\mathrm{n})}$ is the estimate of the kth low resolution image at the nth iteration, and $\mathrm{h}_{\mathrm{xy}}^{\mathrm{BP}}$ is the back-projection kernel that projects the estimation error from the low resolution space to the high resolution one. The iterations stop when some kind of convergence condition is reached (usually until the difference between the current and the previous estimation is lesser then a chosen threshold). This method is conceptually simple, but the solution might not be unique due to the ill-posed nature of the problem.

The **Deterministic Regularized Approach** [54,55,56] overcomes the ill-poseness issue by using some prior knowledge to lead the uniqueness of the solution. The prior knowledge is usually formulated as a smoothness constraint on the estimated solution to prevent an un-physiological high-frequency content. In the case of a constrained least-square regularization the optimal solution is derived from the following problem:

$$\hat{X}_R = argmin\left[\sum_{k=1}^{N} ||Y_k - W_k\hat{X}||^2 + \gamma||C\hat{X}||^2\right]$$

(12)

where $\gamma$ is the regularization parameter and $C$ represents an high-pass filter operator that “measures” the high-frequency content of the estimated solution. If the problem is convex, we can apply a gradient descent algorithm to compute the optimal solution. The main limit of the high-pass filter regularization method is that it may lead to edge alteration of the reconstructed structures. On the other hand, bounds among different tissue are main information content in the MRI images.

The **Statistical Regularized Approach** [57,58] uses a maximum likelihood (ML) estimator to find the high resolution image maximizing the a posteriori probability density function (PDF) $P(X|Y_k)$. Maximizing $P(X|Y_k)$ and computing the natural logarithm the likelihood estimator becomes:

$$X_{MAP} = argmax\left[\ln\left(P(Y_k|X)\right) + \ln(P(X))\right]$$

(13)

This is referred to the Maximum A Posteriori (MAP) method, where $P(X)$ can contain any a priori information on $X$, even multiple constraints (see [55] for instance). The likelihood term $P(Y_k|X)$ is generally modeled as a Gaussian distribution with mean equal to the model prediction $Y_k$ and standard deviation $\sigma_k$ to represent noise residual:

$$P(Y_k|X) = \prod_i \frac{1}{\sigma_k\sqrt{2\pi}} \exp\left(-\frac{(\hat{Y}_k(i) - Y_k(i))^2}{2\sigma_k^2}\right)$$

(14)

where $\widehat{Y_k}$ are obtained based from $\hat{X}$ using eq. 10. Various image priors can be used,the simplest form involves an exponential function that is quadratic in the voxel values, i.e. $P(X) = \exp(-\hat{x}^T Q\hat{x})$ where $Q$ is a symmetric, positive definite matrix, with $Q = C^T C$ where $C$ is the gradient magnitude image operator which measures the structure borders.

**Example-Based Methods** [59,60] hinge on two major factors: collecting a large and representative database of low-resolution and high-resolution image pairs, and learning their mappings. These database are collections of patches (usually 2D), taken from a general dataset or from the same acquisition. A high-resolution patch is then reconstructed from the learned mapping with a relationship 1:1 between high and low resolution patches, or a linear combination of a set of low-resolution patches. These database are usually referred as “dictionaries”. Large dictionaries take into account more information about the possible variations of the high-resolution content, however very large dictionary are very hard to handle from a computational cost prospective.

In [59] a dictionary is constructed from a single acquisition: high-resolution patches are collected from a set taken from the high-resolution stack, while low-resolution patches are chosen on the other two orientations. The mapping is computed using the Nearest Neighbor (NN) criteria, where the high resolution patch is down-sampled using a degradation acquisition model, and they look for the most similar low-resolution patch. Once the 1:1 relationship between the high and the low resolution examples is found, the low resolution images that have to be up-sampled are reconstructed using this mapping. However, this method has the problem of the high computational cost due to the dictionary dimension.

To overcome the computational problem, a sparsity constrain can be applied to generate the dictionary [60]. Given a set of observed vectorized 2D patches $S \in R^{l\times m}$, this can be represented approximately by a sparse linear combination of atoms form a learned overcomplete dictionary $D$, such as $S \sim DA$ where $A \in R^{K\times m}$ is the matrix of coefficients with a few non-zero entries. The dictionary is learned by optimizing the following minimization problem

$$\left(\widetilde{D},\tilde{A}\right) = argmin_{D,\alpha_i}\|s_i - D\alpha_i\|_2$$

(15)

Where $s_i$ are the vectors of $S$, and $\alpha_i$ are the coefficients of $A$. The optimization can be implemented with two procedures: the first is to optimize $A$ with fixed $D$ (sparse coding procedure), the second is to optimize $D$ with a fixed $A$ (dictionary update procedure).

## 3. Proposed method: SRA-T1W

Our method (from here on SRA-T1W) allows to reconstruct a high resolution T2W volume from a bunch of 2D T2W sequences with an high in-plane resolution and a low through-plane resolution, using a T1W sequence of the same subject as a prior constraint to guide the reconstruction. SRA-T1W is an extension of the method proposed in [61]. In particular, in [61] a T1W image of the same resolution of the final reconstructed image is required, thus it is likely that the final resolution of the reconstructed T2W volume will be 1x1x1 mm$^3$. Differently, we extended the method so that the resolution of the reconstructed image could be higher of any input image one, either T2W or T1W. Moreover, the original formulation of [61] handle only one T2W sequence while we extended the method to account also for multiple sequences. This is due to the fact that standard clinical protocols often include a 1x1x1 mm$^3$ T1W 3D image and several T2W images with an in-plane resolution higher than 1x1 mm$^2$. Another important feature of SRA-T1W is the image registration. In most of the SRR works, the problem of the registration between the acquired images and the final high resolution one is not taken into account and registrations are usually assumed to be perfect, claiming that the analysis of the goodness of the SRR is independent from the registration. However, it is well known that the inability to guarantee a perfect registration is a bottleneck for the application of the SRR algorithms [46].

In the following part of this chapter, we will describe the different steps of SRA-T1W for the reconstruction of a high resolution T2W volume. These steps are: *denoising*, *intensity correction and normalization*, *registration*, and *reconstruction*.

***Denoising*** is performed to enhance the SNR of the acquired images. We used a fully-automated algorithm proposed in [59] based on the concept of Non Local means (NL-means) filter originally introduced in [63]. The NL-means filter is defined as:

$$NL(u)(x_i) = \sum_{x_j \epsilon \Omega^3} w(x_i, x_j) u(x_j)$$

(16)

where the restored intensity $NL(u)(x_i)$ of voxel $x_i$ is defined as a weighted average of all the voxel intensities in the image $u$ (or in a subset of it). Weights are computed as:

$$w(x_i, x_j) = \frac{1}{Z_i} \exp\left(\frac{||u(N_i) - u(N_j)||_2^2}{2\beta\hat{\sigma}^2 |N_i|}\right)$$

(17)

where $N_i, N_j$ are small volumes around the voxels $x_i, x_j$, $Z_i$ is a normalization factor, $\beta$ is a free constant parameter that is used to define the smoothness of the image, $\hat{\sigma}$ is the estimate of the noise standard deviation, and $|N_i|$ is the size of $N_i$ (with $|N_i| = (2d+1)^3, d \in N)$. For this application, we used the parameter configuration suggested in [59]. Figure 16 shows the effect of the *denoising* step on an example T2W image. The algorithm well preserves the structural details, see for example the vessels or the edges of the cortical layer, of the putamen and of the caudate. On the other hand, the method also provides an efficient reduction of the noise that can be appreciated in the wide uniform regions in the white matter.

The following step is the ***intensity correction and normalization*** of images. A basic assumption of the resolution enhancement algorithm is that voxels from the same tissue are characterized by the same intensity value, both inside the same image and among different ones. In the real data, this assumption is not always satisfied due, for example, to field inhomogeneities, different voxel volumes or different amplifier gain settings among sequences. To overcome this problem, we performed a two steps intensity correction and normalization operation before applying the reconstruction algorithm. Firstly, we used the N4 bias field correction algorithm [39] to avoid any intensity artifact due to the field inhomogeneity. Figure 17 shows the effect of the N4 algorithm on a sample image.

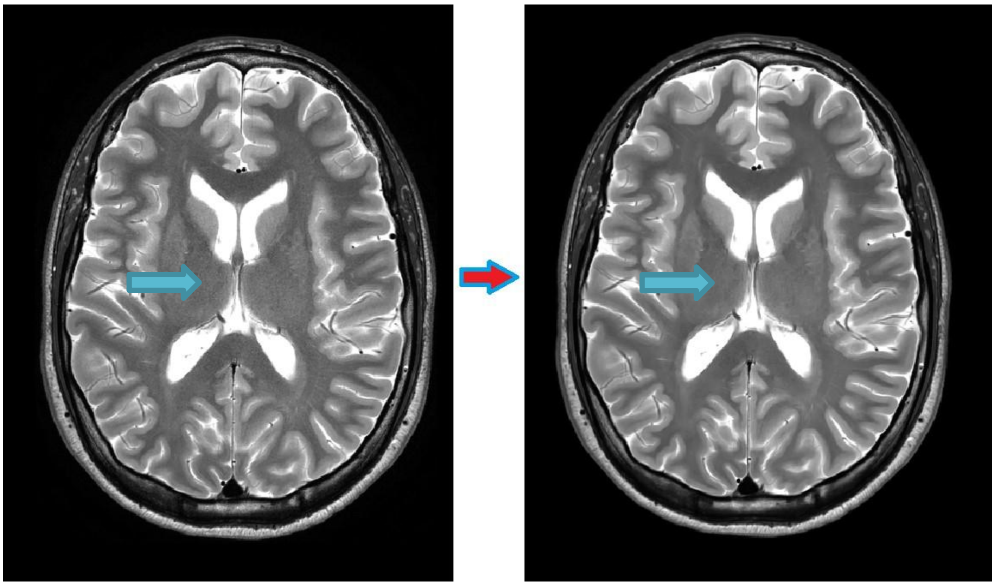

**Figure 16 - Effect of the denoising step on a T2W axial slice. Left: image before performing denoising; right: the same slice after performing denoising. The blue arrow points a region where the denoising effect is more visible.**

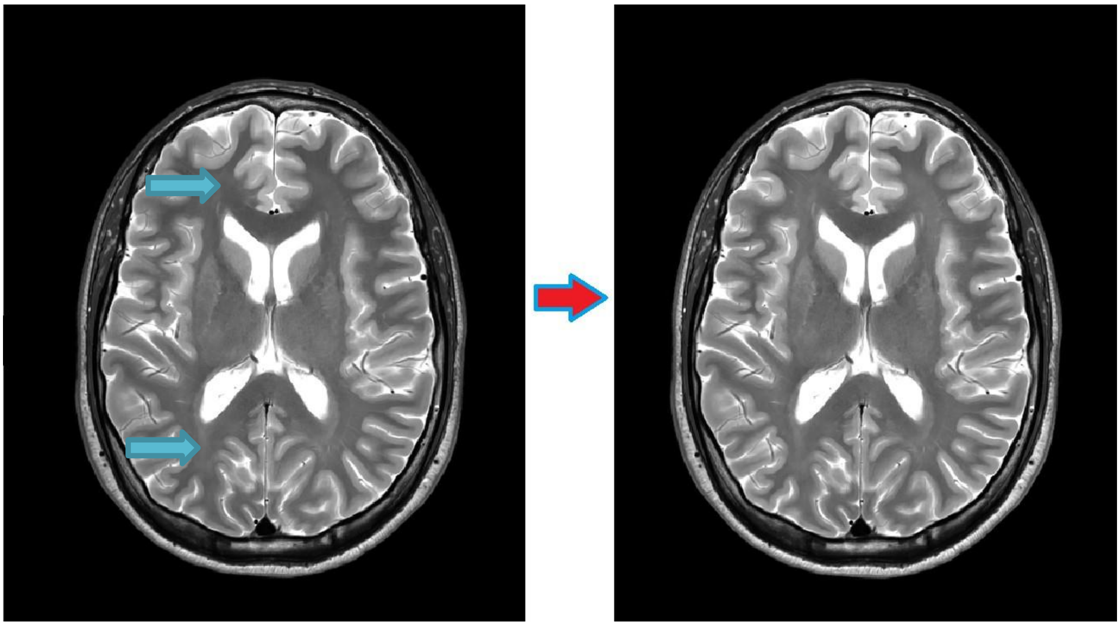

**Figure 17 - Effect of performing N4 bias field correction on a t2W axial slice. Left: slice before the correction; right: the same slice after the correction. The blue arrows point at white matter regions in the frontal and posterior part of the brain. We can see that the white matter has a darker trend in frontal part respect to the posterior one before applying the N4 algorithm.**

Secondly, we performed a between-sequences intensity correction using a linear transformation that changes the voxel values into a range between 0 and 256:

$$x_i = \left(\frac{256}{\max(u)}\right) * x_j \tag{18}$$

where $x_i$ is the corrected voxel and $x_j$ is the original voxel of the image $u$. The same procedure was performed both on the T2W and on the T1W images.

The ***registration*** of the different images is very important for the reconstruction process. In our method the reference space is given by up-sampling the T1W volume to the desired resolution. We choose the T1W volume as reference for all registration operations because it is more reliable about brain structure proportions than a multislice sequence due to its 3D readout. We performed a 12 Degree Of Freedom (DOF) affine transformation to register each T2W image to the T1W one of the same subject. The

affine registration accounts in some measure for the partial volume effect that is present in our data due to the high level of anisotropy of the T2W image voxels. We used ANTs

1.9x-unix [38,39] to perform all registration operations, using the mutual information metric, and a Gaussian regularization operator with sigma equal to 2 on the similarity gradient. All other parameters were left with default values.

The image ***reconstruction*** is the most important step of the method. We used an iterative resolution enhancement method to reconstruct the high resolution volume. Each can be simplified into a two-step procedure: the estimate of the high resolution T2W image and the back-projection of the result to each original low-resolution image space. An initial estimate of the isotropic T2W image is obtained by interpolating the registered volumes on the reference grid. For the initial estimation of the reconstructed volume $\hat{x}^0$ a linear interpolation operation was used to project the low resolution sequences on the high resolution reference space. In [58] it was demonstrated that the choice of the interpolation algorithm doesn't influence the final result in a significant manner. Following the approach proposed in [61], the first step is a filtering operation that apply a two component filter: the first component is a sigma filter that depends on the T1W volume $(z)$, the second component is a NL-means filter regulated by the combined T2W images $(x)$:

$$\hat{x}_p^{t+1} = \frac{1}{C_p} \sum_{\forall q \epsilon \Omega} \hat{x}_q^t \, e^{\left(\frac{-\left(z_p - z_q\right)^2}{h^2}\right)} e^{\left(\frac{-||N\left(x_p^t\right) - N\left(x_q^t\right)||^2}{kh^2}\right)}$$

(19)

The voxel $x_p$ at the iteration t+1 is computed as a weighted sum of the voxels $x_q$ belonging to a neighborhood $\Omega$ of $x_p$. The weights come from the product of two terms, the first one evaluates the similarity between the corresponding voxels in the T1W reference $z$, the second one computes a self-similarity index in the T2W reconstructed volume $\hat{x}^t$ , where $N(x_i^t)$ represents a 3D patch around the voxel $x_i^t$ . $C_p$ is a normalization constant, while $k$ and $h$ are two parameters that control the strength of the filters. The idea behind eq. 19 is that if two closed voxels are similar in the T1W volume, they should be similar also in the corresponding T2W volume and, consequently, the first exponential will increase. On the other hand, if two closed voxels are similar in the estimated T2W image, but different in the T1W volume, it may be due to the fact the acquired T2W images captured a structure that is not visible in the T1W image due to their high in-plane resolution. In such cases, the second exponential term will increase and compensate for the low value of the first exponential term.

The second step of the reconstruction process takes the result from the previous step and back-projects the current estimation of the super resolution T2W volume to the original space of each one of the low resolution volumes. This is done firstly by applying the inverse transformations computed in the registration step, and subsequently using a 1D Gaussian Point Spread Function (PSF) in the slice selection direction to reach the original resolution. The application of a 1D Gaussian PSF function, to decrease the sampling factor and to apply the simulated blur inducted by the acquisition process, has the advantage to take in account non-integer anisotropy ratio to reconstruct volumes at the desired resolution, equal to the in-plane one of the original data. If $v_H$ is a vector of points taken from the slice selection direction on the current high resolution T2W, the 1D Gaussian PSF can be defined with the following operation:

$$v_L(i) = \frac{1}{C_G} v_H e^{\left(-\frac{(x_H - R_{HL} \cdot (j-0.5)^2}{2\sigma^2}\right)} \quad , i = 1, \dots, N_L$$

(20)

where $v_L$ is the vector of points taken in the slice selection direction for the low resolution volume, $x_H$ is a the support vector for the position of points in $v_H$ (corresponding vector for the high resolution volume), $R_{HL}$ is the ratio between voxel dimensions in the high resolution and in the low resolution volume, $C_G$ is the normalization factor, $i$ and $j$ vector indices, and σ is the Gaussian standard deviation, computed so that the FWHM will be equal to the original slice thickness. The resulting low resolution estimates should be equal to the original low resolution T2W volumes. Finally, the differences between the original and the estimated T2W volumes are computed, projected to the high resolution reference space with a linear interpolation and used to update the super resolution image:

$$x^{t+1} = x^{t+1} + \frac{1}{K} \sum_{i=1}^{K} L(\hat{y}_i - y_i)$$

(21)

where $L$ is the linear interpolator operator, $\hat{y}$ is the estimated low resolution sequence, $y$ is the original low resolution sequence, $y$ is the original low resolution sequence and $K$ is the number of low resolution images. These steps are iteratively repeated, using the current estimation in the next step and decreasing the strength of the filter each time, until no significant improvement is obtained (the mean absolute difference between two consecutive reconstruction is lower than a previously defined value). A block diagram of the *registration* and *reconstruction* steps is shown in figure 18.

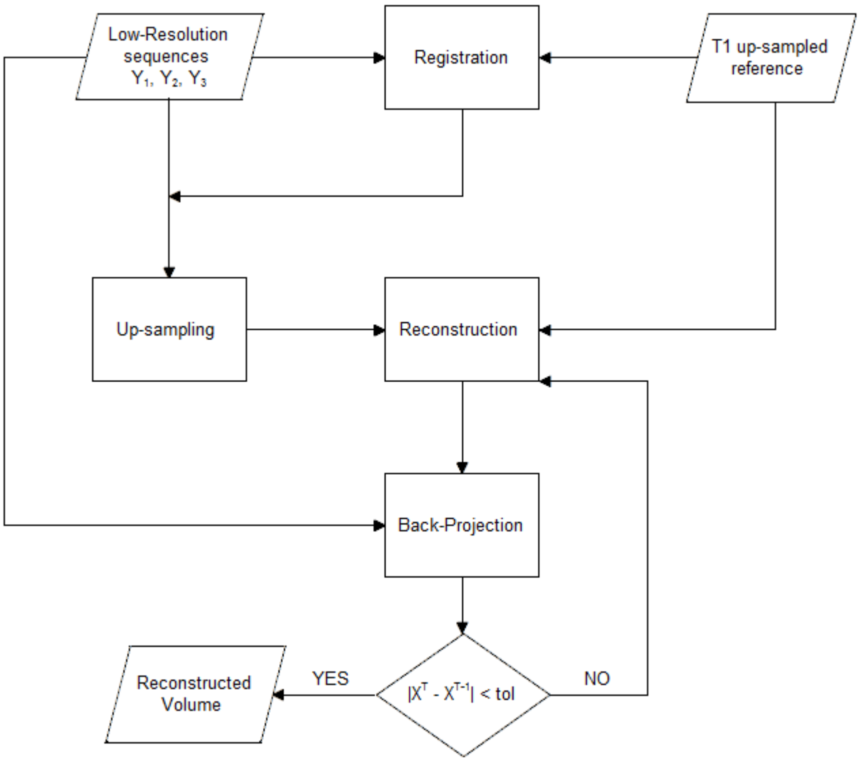

**Figure 18 - Block diagram of the *registration* and *reconstruction* steps. Low resolution images are first registered to the T1W reference and averaged. Then the iterations of filtering and back-projection operation are repeated until convergence is reached**

## 4. Implementation details

The computational complexity is one of the main problem in the contest of SRR methods, because they often involve multiple iterations with big dimension data. In the SRA-T1W method, the first step of the reconstruction procedure is the most expensive in terms of computational time. The factor that mainly influences the computational complexity is the matrix dimension of the volume (i.e. the final resolution), while the computational time of the reconstruction process is almost independent of the number of the input sequences. In our implementation of eq. 19, we shifted both the current reconstructed volume and the T1W reference to simultaneously compute the weights inside the 3D search window $\Omega$ for all the voxels instead of evaluating them one voxel at time. Other free parameters that influence the strength of the filter in eq. 19 are the parameters $h$ and $k$. An high value of the parameter $h$ leads to be a less selective filter, and more voxels will be used for the averaging process. Conversely, if $h$ has a small value only very similar voxels will be considered. The parameter $k$ balances between the amount of information that is taken from the T1W up-sampled reference in comparison and the self-similarity information in the reconstructed T2W volume. If k is too small then only the T2W self-similarity components would affect the filter, thus being more sensitive to the noise in the T2W images. On the contrary, higher values of k polarize the filter action mainly towards the T1W similarity, with a risk of losing the details present in the high in-plane resolution of the input T2W images. In this work, we used decreasing values of $h$ (32,16,8,4, and 2 constant for the following iterations) to enable a coarse to fine behavior of the filter, and $k$ equal to 256 [61]. Finally, the last two parameters are the sizes of the 3D search volume $\Omega$, and the size of the patch used for the similarity measure $N(x_i)$. For this application, we used windows of $7 \times 7 \times 7$ voxels and $3 \times 3 \times 3$ voxels, respectively.

## 5. Experiments

To validate SRA-T1W, we performed the following experiments:

1) a quantitative test on simulated data;

2) a quantitative test on phantom data;

3) a qualitative evaluation on a real MR dataset acquired on a volunteer subject, with 2D-TSE sequences.

The first quantitative experiment allows to evaluate the improvement using three orthogonal T2W sequences, instead of using only a single sequence as in [61]. The phantom data experiment is used to quantitatively assess the accuracy of the final resolution reached by our method, while the third experiment will assess the improvement in terms of structure recognition and delineation on a real brain dataset.

### 5.1 Experiment 1: Brainweb dataset

In the first experiment we used a synthetic dataset of T2W and T1W brain volumes downloaded from the publicly available database Brainweb [64,65]. We used the volumes with $1\times1\times1$ mm$^3$ resolution, and $181\times217\times180$ voxels, without noise or bias field inhomogeneity. This ideal condition was set to compare the performance of the original formulation of the algorithm proposed in [61] with our pipeline. For a quantitative comparison we used the Peak Signal-to-Noise Ratio (PSNR) index:

$$PSNR = 20 \cdot \log_{10}\left(\frac{R}{\sqrt{MSE}}\right) \tag{22}$$

where $R$ is the range of intensity values, and $MSE$ is the mean squared error between the true T2W volume and the reconstructed one. Simulations from the high resolution T2W sequence were obtained through a down-sampling operation with a boxcar function in axial, coronal and sagittal direction respectively, with a down-sampling factor of 7. The reconstruction pipeline was applied to the single coronal, sagittal and axial sequences to reproduce the approach in [61]. Then, all images were used simultaneously as described in our pipeline. Table I shows the PSNR values for all the experiments.

TABLE I

PSNR VALUES

|  | **Linear Interp.** | **SRA-T1W** |  |  |  |
|---|---|---|---|---|---|
|  |  | **Ax.** | **Cor.** | **Sag.** | **Ax., Cor., Sag.** |
| **PSNR** | **18,22** | **24,46** | **29,14** | **26,14** | **33,34** |

**PSNR values of the reconstruction results using 1) the linear interpolation and the mean of all three sequences, 2) Reconstruction proposed in [61] applied to each sequence (axial, coronal, sagittal) independently, and 3) all three sequences.**

As a reference, we computed also the PSNR of the average of the linearly interpolated sequences. All reconstruction approaches perform better than computing the average of the interpolated sequences. Moreover, the SRA-T1W method provides the best overall performance. Figure 19 shows the original data and the reconstructed volumes. SRA-T1W reaches less blurry results compared to the linear interpolation, and details are better reconstructed compared to the use of a single sequence.

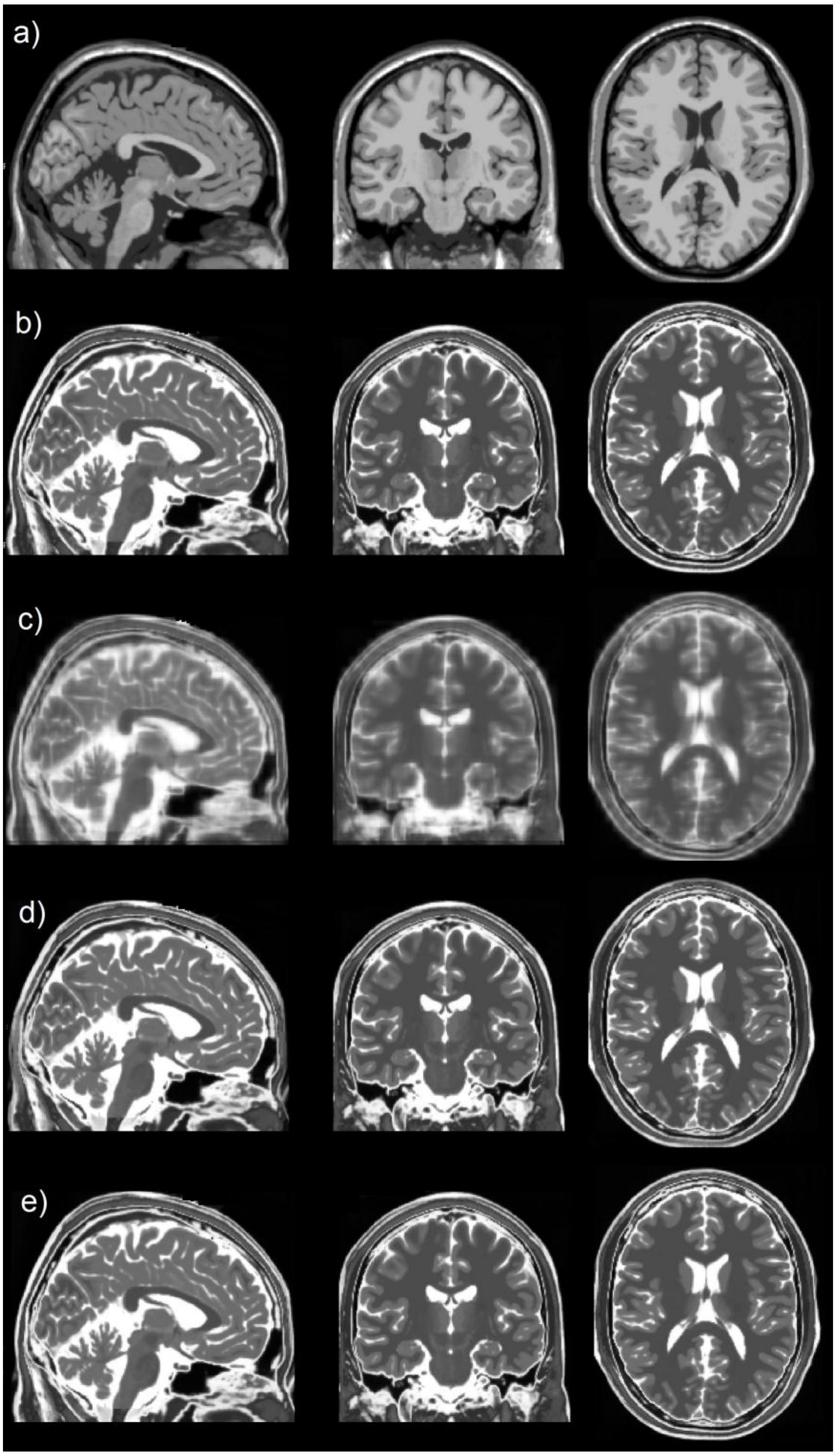

**Figure 19 - Results for the experiment 1 using the Brainweb dataset. The columns give a view of a sagittal, coronal and axial slices respectively. a) T1W reference; b) the true T2W; c) T2W obtained through linear interpolation; d) T2W reconstructed using just the coronal sequence; e) T2W reconstructed with SRA-T1W.**

### 5.2 Experiment 2: phantom dataset

In the second experiment, we tested the ability of SRA-T1W to reach a submillimetric resolution, higher than the acquired 3D T1W reference volume. Data were acquired on a 3 Tesla *Philips Achieva* MR scanner equipped with a 32 channels head coil. We acquired orthogonal sequences of a *Diagnostic Sonar Eurospin II MR Test Object TO04* (*Diagnostic Sonar Ltd*.) phantom that is designed to test the resolution of the acquired images using different bar patterns contained in the phantom (up to 0.3 mm thickness). We acquired a T1W 3D sequence (matrix dimension: $224\times224\times209$, voxel dimension: $1$ mm$^3$, TR: 8 msec, TE: 3.7 msec), and three orthogonal T2W FSE sequences, not collinear with the bar pattern and without gap between slices, with voxel dimension: $0.3\times0.3\times2.25$ mm$^3$, TR = 4.3 s, TE = 80 msec (first sequence matrix dimension: $704\times704\times93$; second sequence matrix dimension: $768\times768\times93$; third sequence matrix dimension: $720\times720\times89$). The final resolution we aimed to reach was $0.3\times0.3\times0.3$ mm$^3$. With this experiment we wanted to demonstrate that SRA-T1W is able to reach a high isotropic resolution, starting from sequences characterized by a voxel size with a high anisotropy degree. Figure 20 shows the results obtained in this experiment. Considering the bar pattern with the lowest distance between bars (0.3 mm), the up-sampled T1W volume is unable to correctly characterize the bar–pattern, showing a region with an almost uniform intensity. The result obtained using the linear interpolation method correctly presents a bar-pattern, but it looks smoothed and blurred. The reconstruction obtained using SRA-T1W clearly shows a bar-pattern, with more defined edges and a wider intensity difference between bars than the other methods. We extracted the intensity profiles along 7 directions perpendicular to the bar layers and average them. Figure 21 reports the average intensity profile for each method. As in figure 20, T1W up-sampling is not able to reconstruct the bar pattern, while the tri-linear interpolation and SRA-T1W correctly show it. Moreover, SRA-T1W provides a wider intensity difference between two consecutive bars than the tri-linear interpolation method. Finally, we computed the Root Mean Squared Error (RMSE) index between the obtained and the ideal bar profiles to compare our reconstruction with the result of the interpolation. Our evaluations show a RMSE equal to 20.00 for the reconstruction using the tri-linear interpolation, and equal to 12.84 for SRA-T1W. The fit of the profiles to the ideal one is also shown in figure 21.

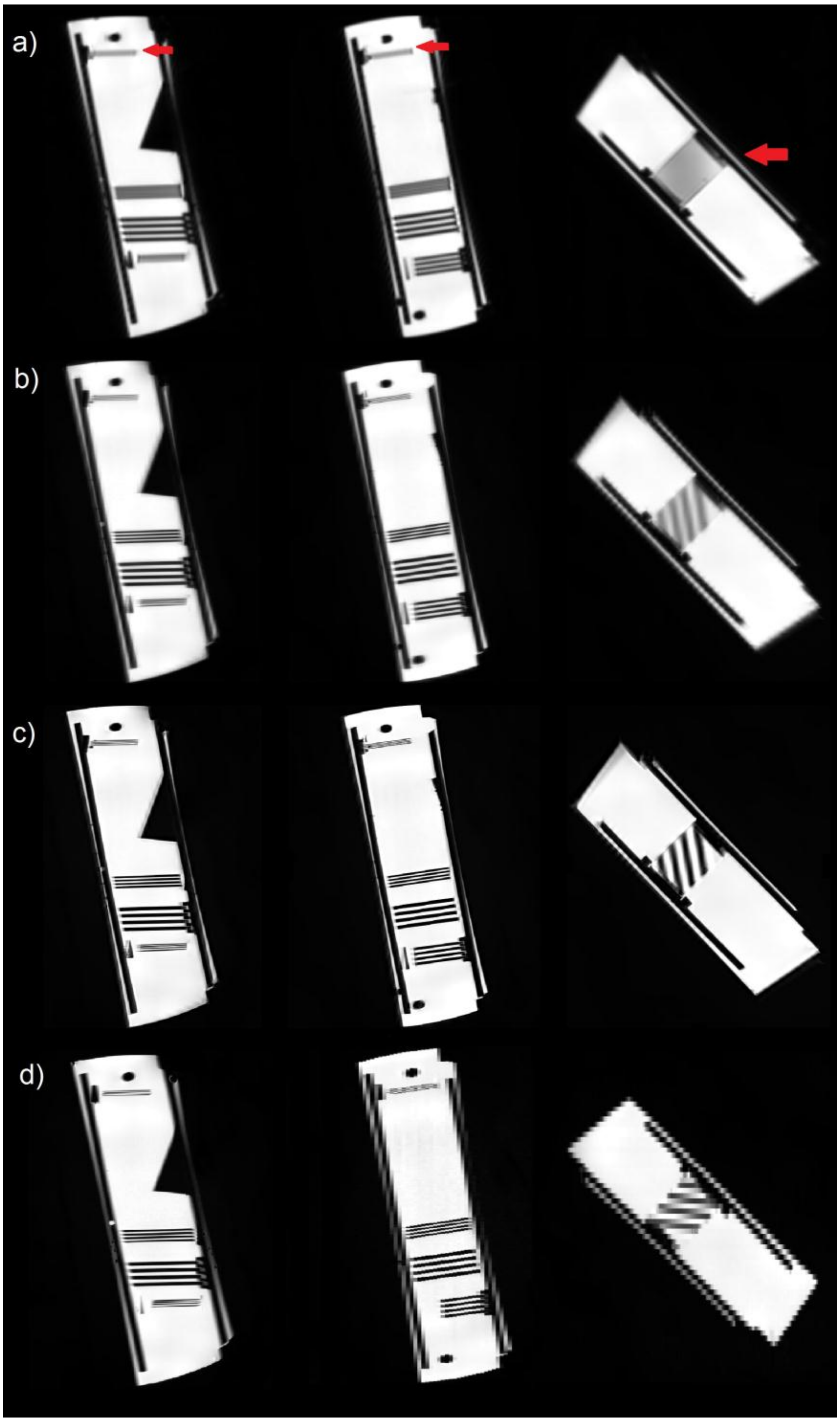

**Figure 20 - Results for the experiment 2 with phantom data: a) the T1W up-sampled reference; b) linear interpolation and average of the three T2W sequences; c) SRA-T1W; d) Example of the original data from one of three acquired T2W sequences. Red arrows show the bar pattern with the highest resolution (0.3 mm).**

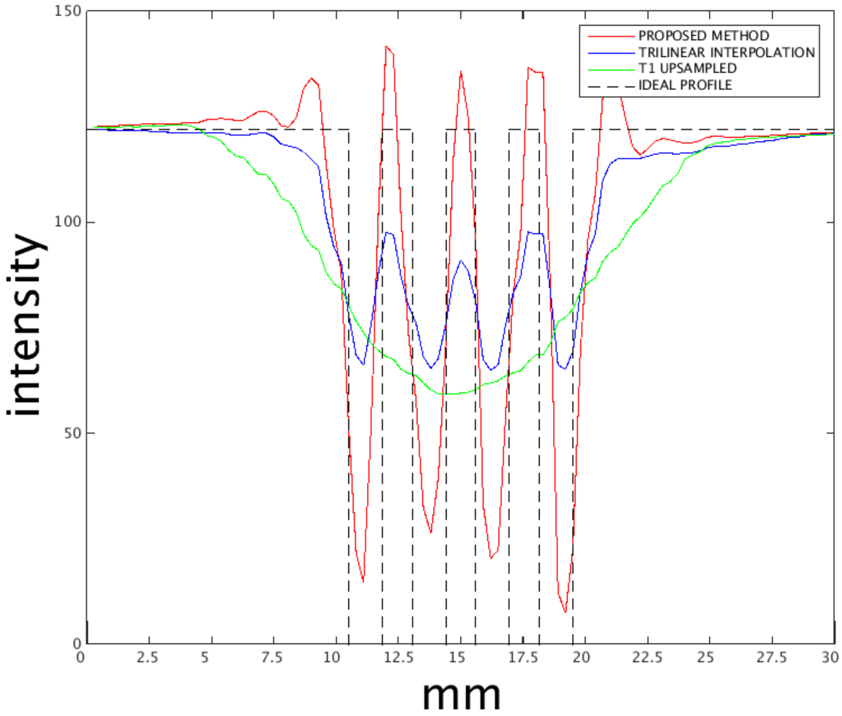

**Figure 21 - Averages of the profiles taken in the normal direction respect to the bar orientation for the bar-pattern with the lowest distance (highest resolution), of 0.3 mm. The profile taken from the T1W up-sampled (green line), from the linear interpolated sequence (blue line) and from the volume obtained with the SRA-T1W (red line). The black dashed line represents the ideal profile of the bar pattern.**

### 5.3 Experiment 3: brain dataset

In the last experiment, we applied SRA-T1W to reconstruct the brain of a normal adult subject, from a set of T1W and T2W sequences part of the routine brain protocol in use at our Institution. Using the same equipment described in the experiment 2 we acquired a T1W 3D sequence (matrix dimension: 256×256×175, voxel dimension: 1 $mm^3$, TR: 8 msec, TE: 3.7 msec), and three T2W FSE orthogonal sequences without gap between slices, TR = 4.2 s, TE = 80 msec and voxel dimension: 0.4×0.4×3 $mm^3$ (axial in-plane matrix dimension: 640×640×46; coronal in-plane with: matrix dimension: 512×512×*62*; sagittal in-plane matrix dimension: 640×640×55). The final voxel dimension obtained through the reconstruction process was 0.4×0.4×0.4 $mm^3$. Figure 22 shows the reconstructed volumes. SRA-T1W provided better results in the delineation of several brain structures (i.e. cerebellar cortex, gray-white matter junction, red nuclei and substantia nigra) with respect to the simple linear interpolation strategy. Figure 23 reports a zoom of the reconstruction result for the cerebellum and for the subtantia nigra. Midbrain cerebellar sulci and folia show less partial-volume effects, while midbrain substantia nigra and red nuclei have sharper borders than the linear interpolation results.

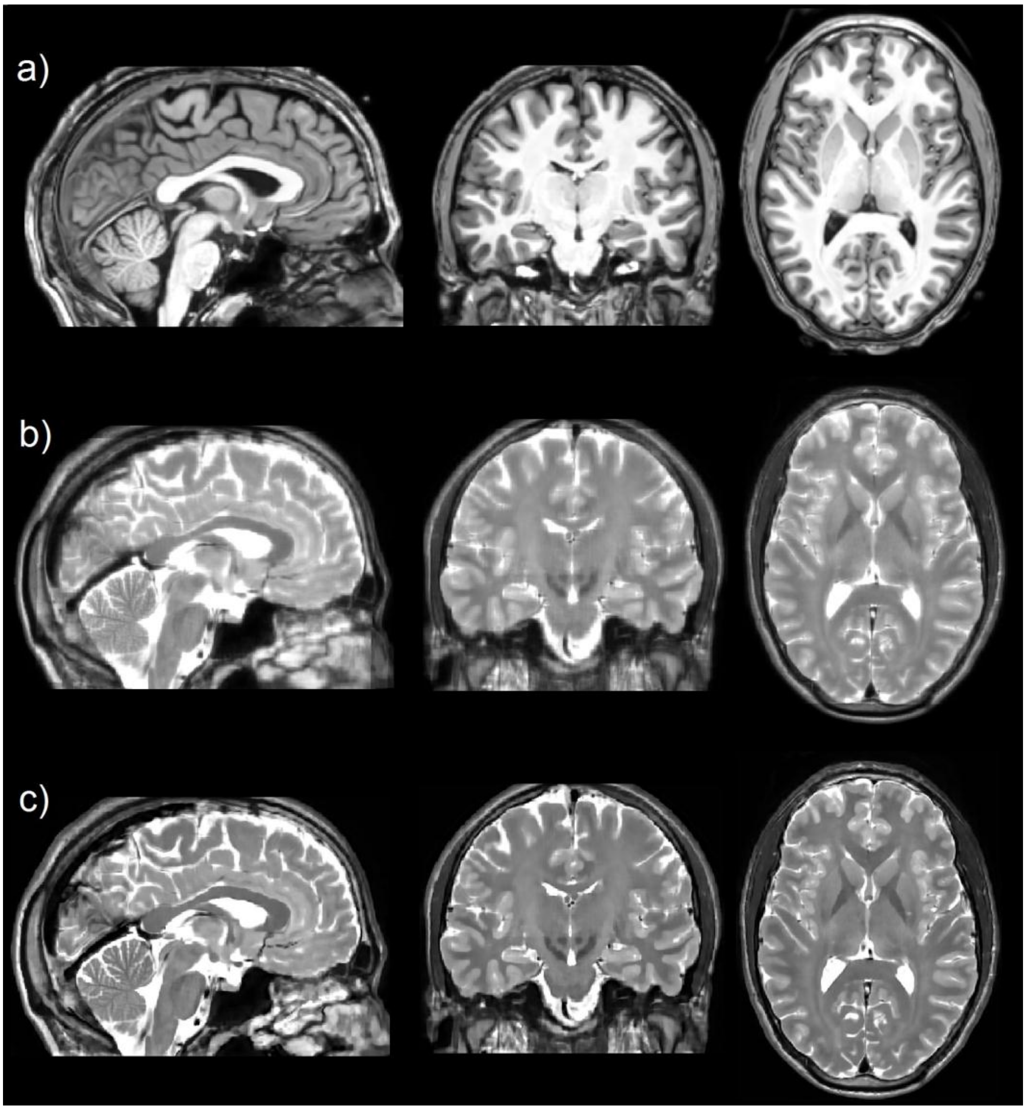

**Figure 22 - Results for the experiment 3 on real MR data. First, second and third columns represent a sagittal, a coronal and an axial view of the same adult normal subject. a) T1W up-sampled reference; b) average of the interpolated T2W sequences; c) SRA-T1W.**

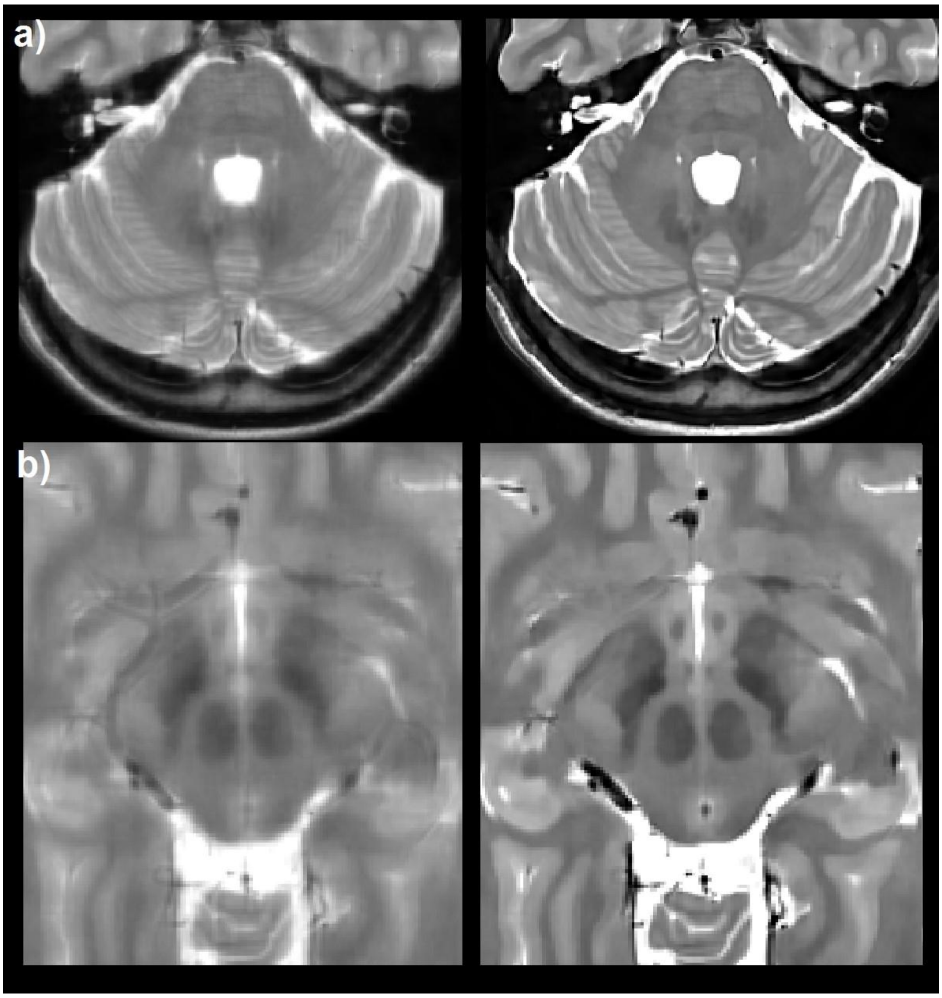

**Figure 23 - Magnification of the cerebellum (row a) and the substantia nigra (row b), obtained through the linear interpolation strategy (first column) and with SRA-T1W (second column).**

## 6. Discussion

In this chapter we presented a complete pipeline to reconstruct T2W isotropic submillimetric resolution volumes from sequences with low through-plane and high in-plane resolutions. Differently from the methods already presented in literature, SRA-T1W already includes the registration operation that is required to integrate the information from multiple T2W images that is usually not accounted for by SRR methods. Moreover, SRA-T1W is very versatile, as it can be applied for sequences obtained with all kind of orientations.

We tested and validated SRA-T1W both on simulated, phantom and human data. Through the experiment on the simulated data we showed that SRA-T1W can reach the desired submillimetric resolution, reconstructing the bar pattern with enough contrast. The experiment with the Brainweb dataset shows that the reconstruction produces a better defined volume, showing higher PSNR values respect to both the simple average of the interpolated input sequences and the reconstruction using just one input sequence. Finally the application of the SRA-T1W on real human data lead to a better visualization of several different brain structures, which are hard to see with less resolved sequences.

Our tests showed also that the use of a T1W reference, even if it is not acquired at the same final resolution, is a good strategy both as a prior for the reconstruction process and as a target for the registration step. T2W high resolution isotropic volumes can be used to perform clinical evaluations with a more complete source of information, thanks to the merging of different acquisitions. Also they are suited to quantitative measurements due to the isotropic nature of the voxels, which reduces the partial-volume error effect. Finally, the resulting reconstructed volumes provide a good reference to perform the EPI distortion correction discussed in the chapter 1. One of the main advantages of the SRA-T1W is that it requires only standard protocol acquisitions to obtain the T2W final volume. No further sequences are required, so the functional EPI can be corrected without increasing the exam duration. As discussed in chapter 1, all the EPI distortion correction methods make use of other supplementary acquisition to perform the transformations: most of all these sequences are useless for every other purposes. The SRA-T1W method, instead, provides a way to avoid additional acquisitions.

The main limitation of our method is that it doesn’t account for inter-slices motion artifacts in the input sequences. The registration step to the T1W consists of an affine transformation, which acts to the whole volume: patient movements during the acquisition can produce mismatches between the slices, leading to artifact in the reconstructed volume. One possible solution can be the implementation of a slice-to-slice or slice-to-volume registration.

# Chapter 3 – Application of the super resolution algorithm to the EPI induced distortion correction problem

## 1. Introduction

In Chapter 1, we presented a new method to correct for EPI induced distortions due to B0 field dishomogeneities. We showed that a non-distorted T2W image can be used to perform deformation-restricted registrations and reach a better match between functional and structural data. In Chapter 2, we showed how the T2W images with an high in-plane resolution can be used to reconstruct an high resolution 3D T2W volume with an isotropic voxel size. The super resolution algorithm was presented focusing on its ability to reach sub-millimetric resolutions, thus being effective for clinical diagnosis and quantitative analyses. On the other hand, such a high spatial resolution is unnecessary to perform the EPI distortion correction in fMRI data, whose resolution is usually over millimetric. In this Chapter, we use our super-resolution algorithm to reconstruct a T2W volume which can be used to perform the EPI distortion correction method presented in Chapter 1 with comparable results with respect to an acquired isotropic T2W image. This approach can answer to common clinical situations, where fMRI dataset are already acquired with no regard of EPI distortion correction and many anisotropic T2W sequences were acquired for clinical purposes. In Chapter 1 we saw that all correction methods need some other support datasets such as the B0 inhomogeneity for the magnetic field mapping methods or an EPI with opposite polarity in the phase-encoding direction for the reversed phase-encoding correction methods. Such acquisitions are hardly included in the clinical practice, due to the fact that their usefulness is limited only for the EPI correction. T2W 2D sequences, instead are often acquired in standard clinical protocol, so in this situation they can be used to generate the support dataset we need for the registration-based correction strategy, while preserving their diagnostic application

## 2. Materials and Methods

*Dataset*

To validate the EPI distortion correction method using a T2W 3D reconstructed volume, we acquired the following dataset:

4 adult subjects (2 male and 2 female);

Sequences: a T1W sequence (TR = 8 msec, TE = 3.5 msec, filp angle 8°, voxel size 1 mm$^3$ isotropic, matrix size $256\times256\times160$) a T2W Fat Suppressed (T2W-FS) scan (TR = 4700 msec, TE = 100 msec, voxel size 1.5 mm$^3$ isotropic, matrix size $160\times146\times110$) a task-fMRI sequence (TR = 2 sec, TE = 20 msec, voxel size $2.5\times2.5\times3.5$ mm$^3$, FOV 240x240 mm$^2$, 40 axial slices interleaved without gap, flip angle 85°, 178 time points) and three T2W turbo spin echo (T2W-TSE) orthogonal sequences without gap between slices, TR = 4.2 s, TE = 80 msec and voxel dimension: $0.4\times0.4\times3$ mm$^3$ (axial in-plane matrix dimension: $640\times640\times46$; coronal in-plane with: matrix dimension: $512\times512\times62$; sagittal in-plane matrix dimension: $640\times640\times55$).

The fMRI protocol used in this validation included a standard block design finger tapping task using both hands, where subjects were asked to press the buttons of a MRI-compatible response-device using all the fingers in sequence from the thumb to the little finger, always starting from the thumb. Blocks lasted 20 sec for each hand with 16 sec inter-stimulus interval, 6 blocks for each hand. The fMRI task was paced according to the screen commands that were provided with a regular pattern. Subjects were trained before the scan to get familiar with the screen commands, hand devices and ensure comprehension of the task.

*Image analysis*

T1W and T2W intensity inhomogeneity were corrected with the algorithm N4 implemented in ANTs [38,39]. Subsequently, T1W and T2W-FS volumes were skull stripped with BET [40] implemented in FSL. Functional volumes were realigned using a rigid transformation, to the first volume of the sequence and then to the average EPI. We used the super resolution method proposed in Chapter 2 to reconstruct a T2W volume with the same resolution of the acquired T2W-FS sequence starting from the clinical T2W-TSE sequences. With this method we can reconstruct a 3D isotropic T2W reference, choosing the final resolution up to the in-plane resolution of the acquired sequences provided as input to the method. We decided to reconstruct a T2W volume at the same resolution of the acquired T2W-FS to better compare the two approaches, avoiding possible confounding effects due to a disparity between qualities. Finally, the reconstructed volume was then slightly smoothed (Gaussian kernel filter with FWHM = 0.5 mm) to reduce any intensity spike that may occur in the reconstructed volume.

We applied the EPI correction method proposed in Chapter 1 twice, using as reference:

1) the acquired T2W-FS (voxel size = 1.5 mm$^3$)

2) the reconstructed T2W volume (voxel size = 1.5 mm$^3$)

As the distortion correction method performs better using the brain image in place of the whole head one, both reference images were masked using BET. As previously described in chapter 1, all registration operations were performed with ANTs, with the exception of the realignment step that was performed with the MCFLIRT tool [41] implemented in FSL. For both the pipelines, the appropriate transformations were combined to perform a single tri-linear interpolation, thus minimizing the interpolation errors. The final resolution of the functional data in the T1W space was 2 mm$^3$. Single subject analysis with SPM12 [42] was performed in the T1W space, and a 3D Gaussian spatial filter with FWHM equal to 6 mm was applied before the GLM. The design matrix included 2 regressors, one for the right hand and one for the left hand movements, computed convolving a boxcar function and the canonical haemodynamic response, and 6 movement parameter regressors (obtained from the functional realignment step) as confounder factors. Also outlier volumes where included as regressors: this was done evaluating the global intensity mean of the 4D fMRI sequence, and excluding volumes which exceeded the average intensity of at least 5 z-score, or moved more than 2 mm. The preparation of the regressors was done using the Artifact detection Tool (ART) [43].

We generated 4 different contrast effects for each pipeline:

1) Right hand movement > Baseline (Rest)

2) Left hand movement > Baseline (Rest)

3) Right hand movement > Left hand movement

4) Left hand movement > Right hand movement

Contrasts 3 and 4 were computed to localize brain regions involved in specific motor functions, while contrasts 1 and 2 estimate the effect of the task with respect to the rest condition.

*Pipeline comparison*

We firstly performed a visual inspection of the activation maps obtained with the different contrasts. Then, we performed a correlation analysis between beta values of the GLM analyses to see what is the impact of the preprocessing pipeline on the final beta maps. We considered the betas from the whole brain, regardless of the activation maps that can be derived from the different contrasts. Finally, a direct comparison of the registrations between functional volumes to the corresponding anatomical T1W is evaluated for each subject computing the percentage difference between the functional volumes obtained with the two pipelines.

## 3. Results

Figure 24-27 show the brain activations generate during the finger tapping task for the subjects, both for the pipeline using the acquired T2W-FS and using the reconstructed T2W volume to perform the EPI distortion correction. Significance was set at $p < 0.05$ corrected with FWE as implemented in SPM12 with no minimum cluster size threshold. Activations are located in the primary motor cortex (precentral and postcentral gyrus) and cerebellar cortex brain regions bilaterally. All subjects included in this experiment present quite similar activation patterns between them. At a visual inspection, this result suggests that the patterns of activation between the pipelines are quite similar.

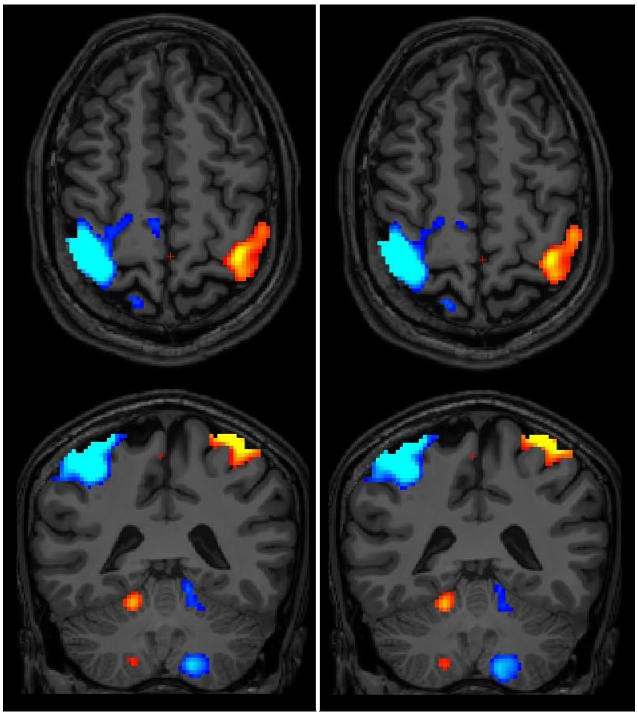

**Figure 24 - Effect of contrast 3 (Red/yellow) and contrast 4 (Blue/white) for subject 1 in radiological convention. Left column: pipeline using the T2W FS volume; Right column: pipeline using the reconstructed volume. Top: axial slice; Bottom: coronal slice. Activations using a significance of p<0.05 corrected with FWE.**

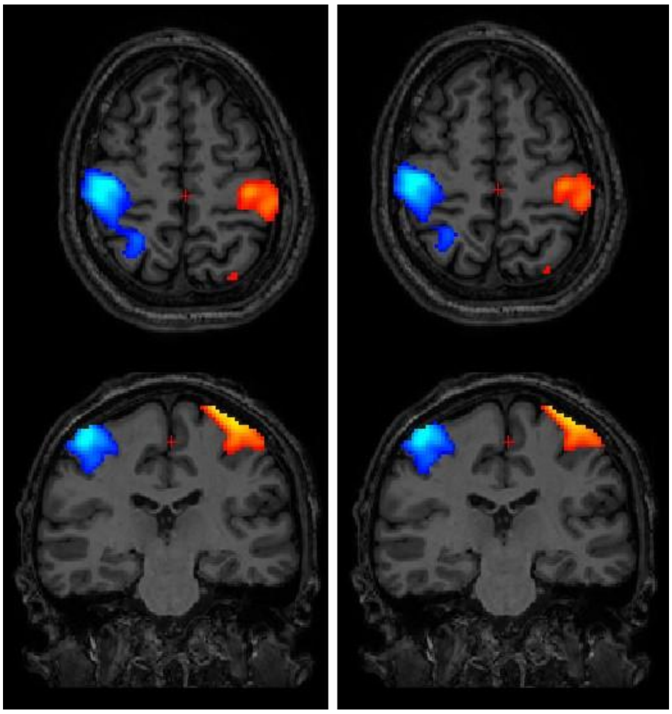

**Figure 25 - Effect of contrast 3 (Red/yellow) and contrast 4 (Blue/white) for subject 2 in radiological convention. Left column: pipeline using the T2W FS volume; Right column: pipeline using the reconstructed volume. Top: axial slice; Bottom: coronal slice. Activations using a significance of p<0.05 corrected with FWE.**

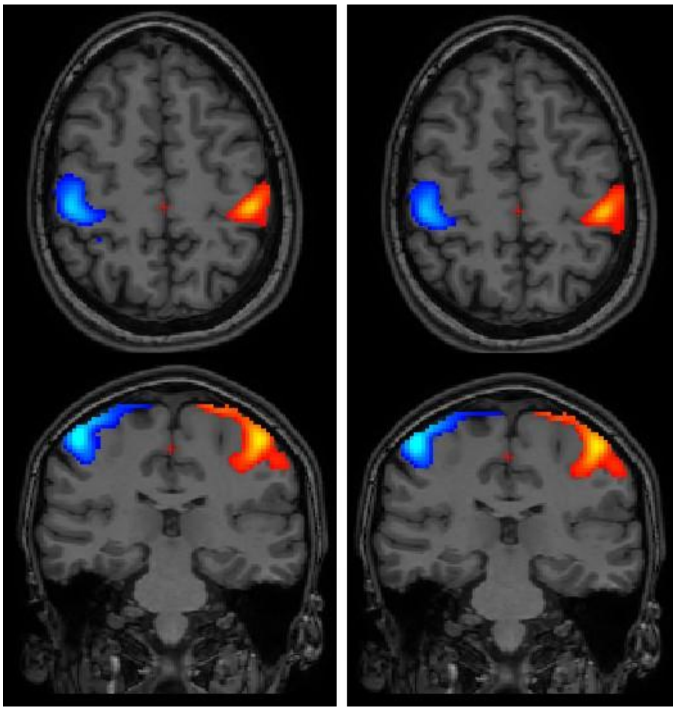

**Figure 26 - Effect of contrast 3 (Red/yellow) and contrast 4 (Blue/white) for subject 3 in radiological convention. Left column: pipeline using the T2W FS volume; Right column: pipeline using the reconstructed volume. Top: axial slice; Bottom: coronal slice. Activations using a significance of $p<0.05$ corrected with FWE.**

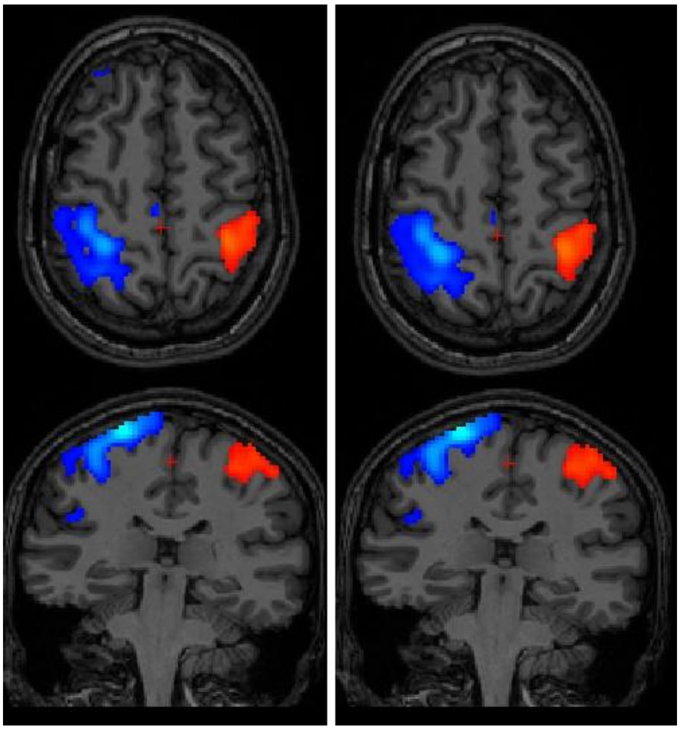

**Figure 27 - Effect of contrast 3 (Red/yellow) and contrast 4 (Blue/white) for subject 4 in radiological convention. Left column: pipeline using the T2W FS volume; Right column: pipeline using the reconstructed volume. Top: axial slice; Bottom: coronal slice. Activations using a significance of $p<0.05$ corrected with FWE.**

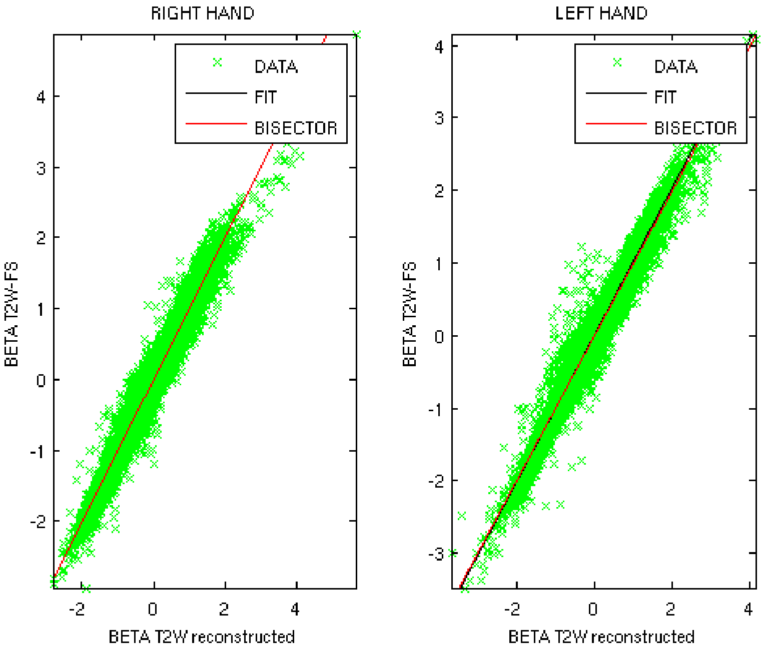

**Figure 28 - Subject 1: Scatter plot of beta values from the two pipeline for right and left hand movements. The black lines show the linear fit between them, while the red lines represent the bisector and so the identity relationship.**

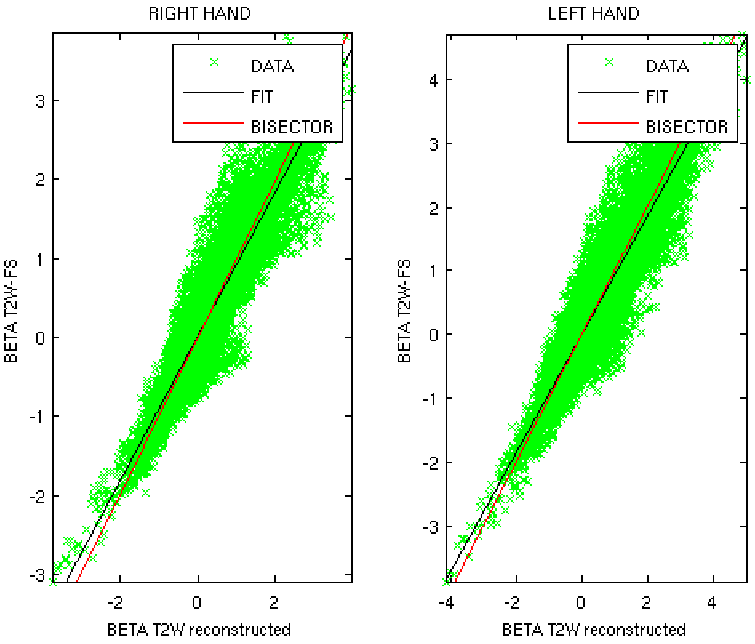

**Figure 29 - Subject 2: Scatter plot of beta values from the two pipeline for right and left hand movements. The black lines show the linear fit between them, while the red lines represent the bisector and so the identity relationship.**

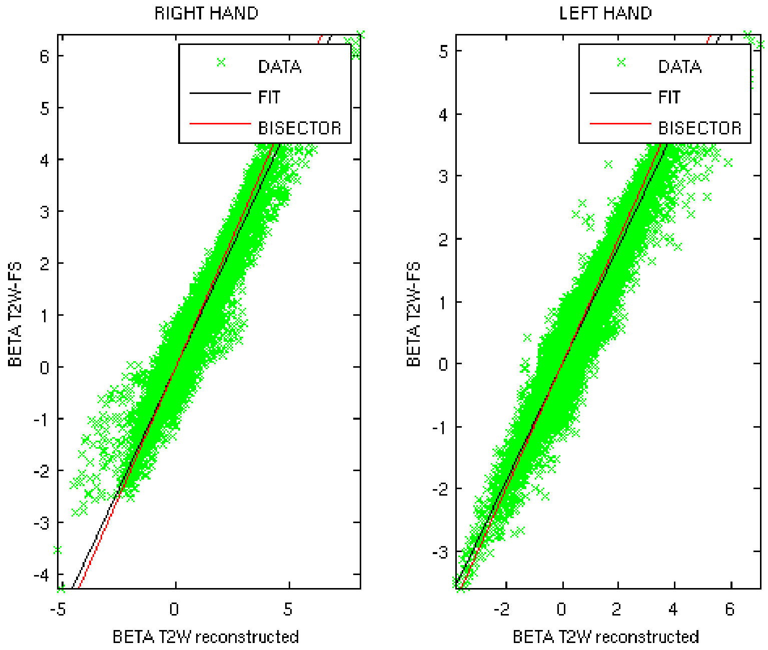

**Figure 30 - Subject 3: Scatter plot of beta values from the two pipeline for right and left hand movements. The black lines show the linear fit between them, while the red lines represent the bisector and so the identity relationship.**

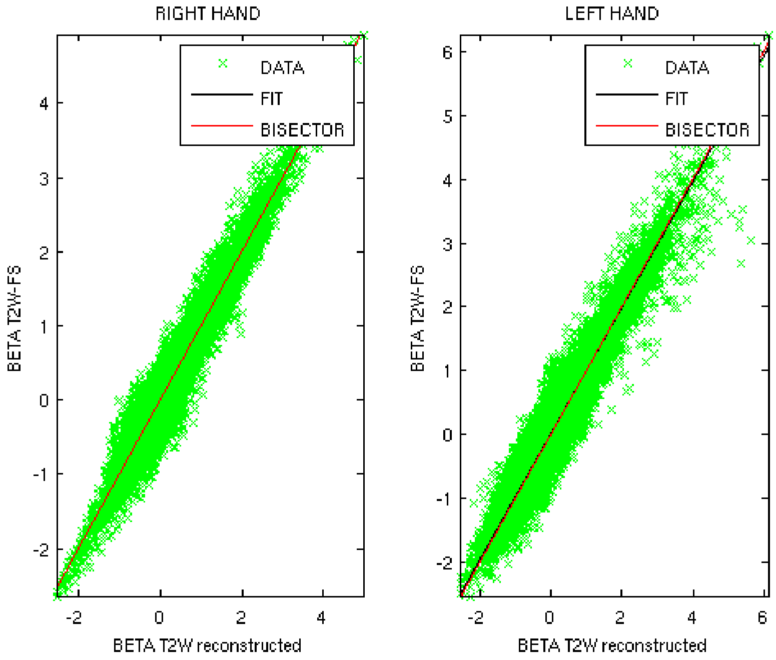

**Figure 31 - Subject 4: Scatter plot of beta values from the two pipeline for right and left hand movements. The black lines show the linear fit between them, while the red lines represent the bisector and so the identity relationship**

TABLE II

CORRELATION COEFFICIENTS

| | **$r^2$ - CONTRAST 1** | **$r^2$ - CONTRAST 2** |
|---|---|---|
| **SUBJECT 1** | 0.97 ($p<0.001$) | 0.97 ($p<0.001$) |
| **SUBJECT 2** | 0.93 ($p<0.001$) | 0.93 ($p<0.001$) |
| **SUBJECT 3** | 0.96 ($p<0.001$) | 0.95 ($p<0.001$) |
| **SUBJECT 4** | 0.96 ($p<0.001$) | 0.96 ($p<0.001$) |

**$r^2$ coefficients between beta values, for each contrast/subject**

Figures 28-31 show the scatter plots and the fit of beta values for both left and right hands for each subject computed on the whole brain. The relationships between parameters are clearly linear, and also approximately corresponding to the identity (bisector line). In Table II we reported the $r^2$ coefficients of the correlations, showing a really high concordance between betas ($r^2>0.93$ with $p < 0.001$ for all the couplings).

The comparison between functional data registrations is shown in Figure 32. Only absolute percentage differences higher than 5% are shown using the subject T1W volume as background. Most of the differences are located on the borders of the brain, or in CSF locations for all subjects. On the contrary, gray matter does not seem to be affected by the choice of the T2W.

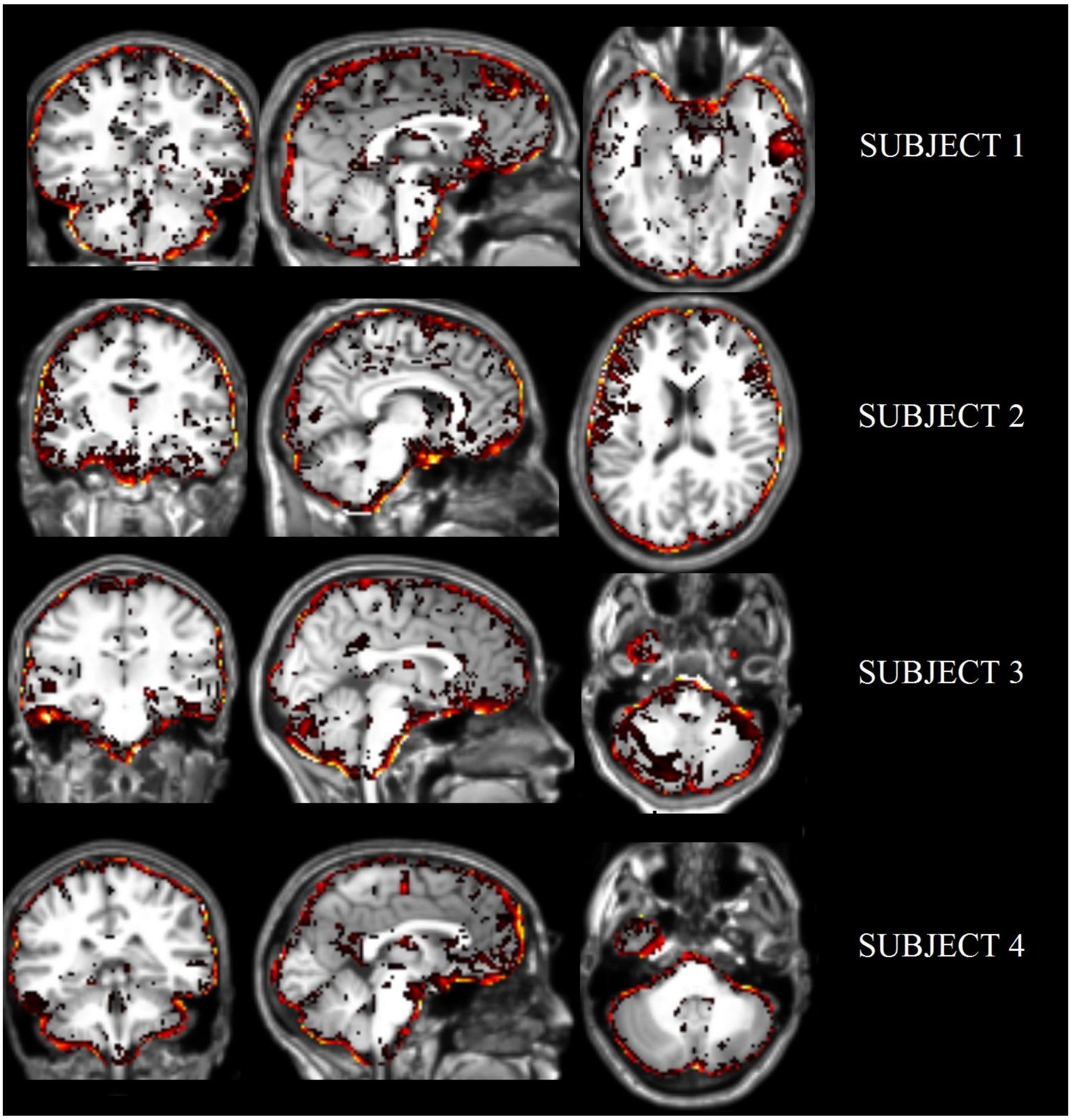

**Figure 32 - Absolute percentage difference between the average functional volumes registered to the T1W using the two pipelines. Results are superimposed on the corresponding T1W volumes, displayed in radiological convention. Only differences upper than 5% are shown, with brighter colors for higher differences. Each row correspond to a subject. We can see that most of the differences are located on the borders of the brain in the CSF.**

## 4. Discussion

In this Chapter we validated the use of our super-resolution algorithm proposed in Chapter 2 to reconstruct a T2W volume, which can be used to perform the EPI distortion correction method presented in Chapter 1. This approach can be applied in common clinical situations, where fMRI datasets were already acquired with no other support acquisition accounting for the EPI distortion (e.g. the B0 field map or the reversed phase encoding EPI images). Such acquisitions, in fact, are hardly included in the clinical practice, due to protocol time constraints and to the fact that their usefulness is limited to the EPI correction operation. Conversely, T2W sequences with a high in-plane resolution are often acquired in standard clinical protocols. Our experiments showed that comparable results can be reached using a dedicated sequence, as the T2W FS image we usually acquire, or the T2W reconstructed using the super resolution algorithm. Both the visual inspection of the activation patterns and the quantitative analyses (beta correlations and percentage differences in the registrations), the two approaches lead to very similar results. Differences in mean functional volumes are mainly located in CSF regions which aren't characterized by the BOLD effect. This is shown also by the correlations between beta values, which are very high, reflecting an high concordance between gray matter regions between the two functional datasets.

In our pipeline (see Material and Methods section) we applied a low level smoothing (Gaussian kernel with FWHM = 0.5 mm) before using the T2W reconstructed volume. This was done to remove intensity spikes in the reconstructed volume, which could lead to wrong registrations between functional and anatomical data. When we acquire a dedicated sequence, as the T2W-FS, we prefer a fat suppressed one to avoid high intensity spikes due to the fat signal. Finally, in our experiments we saw that using the full volume, without performing the brain extraction step, could lead to misalignment due to the scalp, which is completely present in the reference volume and suppressed in the functional data. Thus, we recommend to always perform this preprocess step to the T2W reconstructed volume before applying the EPI correction method.

# Chapter 4 – Clinical Studies

## 1. Introduction

In this chapter we will explore some clinical studies where the method of the EPI distortion correction was successfully employed. All these studies were conducted in the research institute Eugenio Medea “La Nostra Famiglia” (LC, Italy) and MRI dataset were acquired with a 3T Philips Achieva scanner.

## 2. Friederich Ataxia dataset

Friedreich's ataxia (FRDA) is an autosomal recessive progressive hereditary neurodegenerative disorder caused by a GAA repeat expansion in the first intron of *FX*N gene on chromosome 9 (Campuzano et al., 1996). FRDA is characterized by a set of motor and sensory deficits resulting in the “ataxic behavior” (Harding et al., 1983).

For this study, a total of 20 patients with confirmed FRDA diagnosis were included for the MRI session. A group of age and sex matched healty control subjects (HCs) was scanned with the same MRI protocol. Patients and HCs underwent an MRI session with a 3T Philips Achieva Scanner (Philips Medical System, The Netherlands), equipped with a digital 32 channels head coil. The acquisition protocol included a T1W high resolution sequence ($T_E/T_R$=3.5/8 msec, flip angle 8°, SENSE factor 2, voxel-size 1x1x1mm$^3$ matrix size 256x256x160), a T2W fat suppressed scan (to perform the EPI distortion correction method, $T_E/T_R$=100/4700 msec, SENSE factor 2, voxel-size 1.5x1.5x1.5mm$^3$, matrix size 160x146x110), and a fMRI sequence (FOV = 240x240mm$^2$, 40 slices interleaved without gap, voxel size 2.5x2.5x3.5mm$^3$, $T_E/T_R$=20/2000 msec, flip angle 85°, 178 time points).

The fMRI protocol included a standard block design finger tapping task using both hands, where subjects were asked to press the buttons of a MRI-compatible response-device using all the fingers in sequence from the thumb to the little finger, always starting from the thumb. Blocks lasted 20 sec for each hand with 16 sec inter-stimulus interval. The fMRI task was paced according to the screen commands that were provided with a regular pattern. Subjects were trained before the scan to get familiar to the screen commands, the hand device and ensure comprehension of the task.

Data were pre-processed using SPM12 and ANTs. Functional volumes were realigned using a two-step realignment process (to the first volume of the sequence and then to the mean volume), than the mean volume was co-registered to the T2W anatomical volume using the method of EPI distortion correction explained in chapter 1. The T2W volume was rigidly aligned to the corresponding T1W anatomical volume that was normalized to the MNI152 space. Finally all these transformations were combined together to avoid further interpolation errors. The combined transformation was applied to normalize the functional sequence on the MNI space, with a final voxel size of 2 $mm^3$. Before the single-subject analysis, a Gaussian spatial filter, with FWHM equal to 6 mm, was applied to the functional data to increase the Signal-to-Noise-Ratio (SNR) and to deal with the residual anatomical differences between subjects. Also an high-pass temporal filter with cut-off frequency of 128 sec was used to correct for slow signal drifts. The GLM approach was adopted to compute the single-subject analysis: the design matrix included one regressor for each state (rest, right hand movement, left hand movement), 6 regressors for the rigid parameter of the realignment process, and one regressor for each outlier volume. A volume was labeled as an outlier if it corresponded to a motion greater than 2mm, or on the basis of the intensities values (spikes). To create regressors and detect outliers, we used ART [43]. After the estimation of the model, we created a map for each effect we wanted to test. To exclude confounding factors due to the non-motor component of the task (attention, visual stimulation) we created contrast maps between the right and the left hand movement task (Right>Left and Left>Right). These maps were then used as inputs for the following GLM group analysis. A two-sample t-test was performed with SPM12 to verify differences between groups using a threshold $p<0.05$ corrected for the False Discovery Rate (FDR). Figure 33 shows a significant higher activation of the left cerebellum cortex, during the movement of the non-dominant hand (left) for the control group respect to the patients. No significant difference was seen during the movement of the dominant (right) hand.

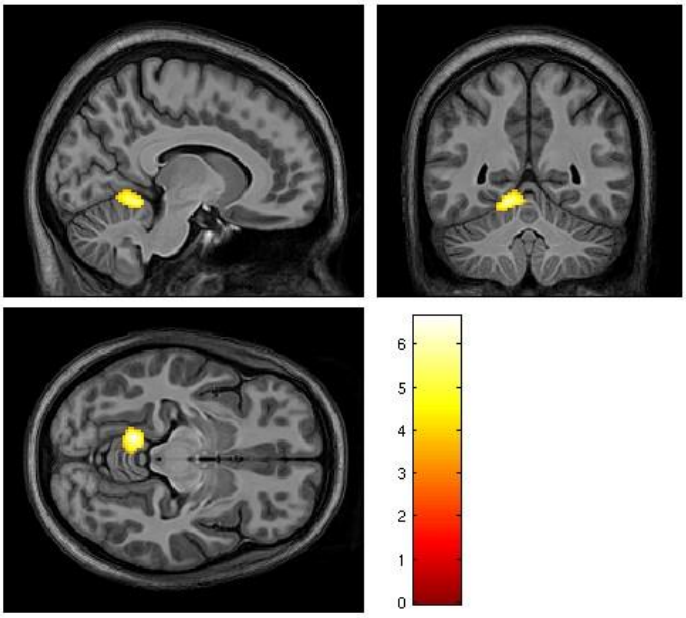

**Figure 33 - Two groups t-test result. Controls have a significant higher activation (p<0.05 FDR corrected) of the left cerebellum cortex compared to the patients.**

To evaluate the impact of the pipeline proposed in this thesis, we computed the same steps described above without using the T2W volume to perform the EPI distortion correction. In this experiment, we directly registered the mean functional volume to the anatomical T1W using a simple affine transformation, then we used the same transformations for all the other steps. In this case, the t-test didn’t show any significant (p<0.05 FDR corrected) different clusters between groups.

## 3. Williams Syndrome dataset

Williams Syndrome (WS) is a developmental disorder that affects many parts of the body. This condition is characterized by mild to moderate intellectual disability or learning problems, unique personality characteristics, distinctive facial features, and heart and blood vessel (cardiovascular) problems. WS is caused by the deletion of genetic material from a specific region of chromosome 7. The deleted region includes 26 to 28 genes, and researchers believe that a loss of several of these genes probably contributes to the characteristic features of this disorder [66].

Resting-fMRI scans were acquired in 9 patients affected by WS and 18 age and sex matched healty controls. The acquisition protocol included a high resolution T1W MPRAGE sequence (voxel resolution 1x1x1mm$^3$ , matrix size 256x256x160, TE/TR 3.86/8.40 msec, SENSE 2), a T2W TSE sequence to perform EPI distortion correction (voxel resolution 1.5x1.5x1.5mm$^3$, matrix size 160x146x110, TE/TR 100/4700 msec, SENSE 2, SPIR fat suppression) and a resting state T2*-W single-shot echo-planar sequence (voxel resolution 2.5 x 2.5 x 4 mm$^3$, matrix size 96 x 96 x 30, TR/TE = 2000/30 msec, 250 dynamic scans, flip angle = 90°) where subjects were instructed not to move inside the scanner and were encouraged to keep calm with closed eyes.

Both T1Wand T2W data were processed with the N4 tool of ANTS to mitigate the intensity inhomogeneity bias, then skull removal was performed with the FSL tool BET. Functional volumes were slice time corrected with SPM12 and realigned with MCFLIRT of FSL. The average volumes of the resting-fMRI realigned sequences were registered to a common anatomical space by a three step procedure. (1) EPI distortion correction method performed on the average fMRI using the corresponding skull-stripped T2W volume; (2) rigid registration between T2W and T1W; (3) an affine and non-linear registration between T1W and MNI reference. To achieve a better match between anatomical structures between subjects in the standard space, a study template was created using the average averaging the mean functional EPI in MNI space: this template was used as a reference for the second registration between EPI in the native space and the template in the MNI space. The mean signal in CSF, WM, the signal drift and motion parameters obtained during the realignment step were regressed out in the native space, then a band-pass temporal filter (0.008 – 0.1 Hz) was applied to remove

physiological and non-BOLD related effects. Functional sequences were then normalized (with voxels resampled at 3 $mm^3$) and smoothed with a Gaussian spatial filter (FWHM = 5 mm). Group analysis was conducted by applying the Independent Component Analysis (ICA) as implemented in FSL MELODIC software, by multi- session temporal concatenation. An automatic procedure estimation was used to select
24 ICA group-components. The selection of “good” and “bad” components (i.e. components related to neural activity and components related to noise/artifacts) was done by visual inspection of: the spatial patterns of ICA maps, and the power spectrum of the time-courses. This procedure led us to label 16 components as related to Resting State Networks (RSNs). Using the dual regression method [67], we used this set of group-average spatial maps to generate a corresponding set of subject-specific spatial maps and time-series for each subject. We then obtained one spatial ICA map and one time signal for each subject and each group-ICA component. These spatial maps and time-series were then fed to further analysis.

We tested for group differences in within network functional connectivity (FC), i.e. how brain regions are more or less involved into a specific network, using FSL’s randomize permutation test tool, applied to the subject-specific ICA-specific spatial maps. For the intra-network FC analysis we adopted a threshold of $p < 0.05$ corrected for multiple comparisons. Figure 34 shows the within FC differences between groups, superimposed on the corresponding ICA group maps. These results show how there are significant differences between HC and WS populations in most of the parieto-occipital brain regions for a set of rs-network. Most of the difference have a clear direction (HC>WS) with the exception of the precuneus region where the direction is the opposite one (WS>HC).

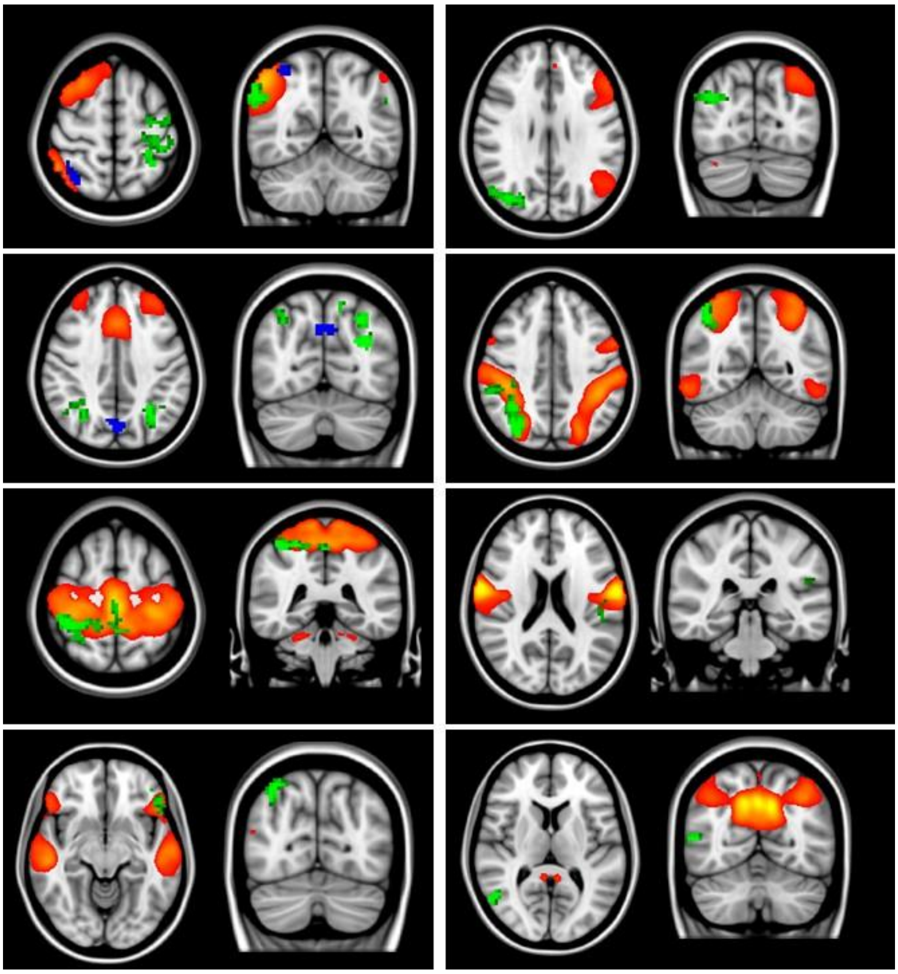

**Figure 34 - Within FC results showing significant ($p<0.05$ multiple comparison corrected) component differences between WS and HC with respect to the corresponding ICA network (red/yellow blobs). Green regions: higher involvement in HC group compared to the WS group (HC>WS). Blue regions: higher involvement for the WS group compared to the HC group (WS>HC).**

# 4. Single-Subject Cerebellum Agenesis

In this study, the case of a 48-year-old right-handed man with a near-total absence of the cerebellum was examined with the aim of understanding the long-term reorganization of a brain developed without a cerebellum [68].

Neuroimaging evaluation was performed using the same 3T scanner of the previous studies. Conventional (T1, T2-weighted, and steady state free precession) and functional (resting-state fMRI) data were acquired both for the patient and a group of age comparable healty adult subjects.

fMRI and structural images were pre-processed using FSL and Advanced Normalization Tools (ANTs). Pre-processing of functional sequence included motion correction, EPI distortion correction with the T2W volume, registration to the T1W image, normalization to the standard MNI space, resampling to 2 $mm^3$ spatial resolution, brain extraction, and Gaussian spatial smoothing (FWHM = 5 mm). A group independent component analysis using the Group ICA Toolbox was carried out. All participants' data were temporally concatenated and 40 independent components were extracted using the FastICA algorithm [69]. Then, group components were retroprojected for each participant and converted into a z-score. Correlation coefficients were calculated for each reliable component and differences between patient and controls were computed using a two-sample t-test ($p < 0.001$).

The analysis of resting-state fMRI data (Fig) easily shows in the patient all main networks usually present in healthy individuals. Auditory, visual, somatosensory, default-mode, and executive-function networks were clearly represented; the executive-control network, which involves the dorsolateral and ventrolateral prefrontal cortex areas, in turn strongly connected with the cerebellum through the frontopontine fibers was significantly different from that in healthy individuals.

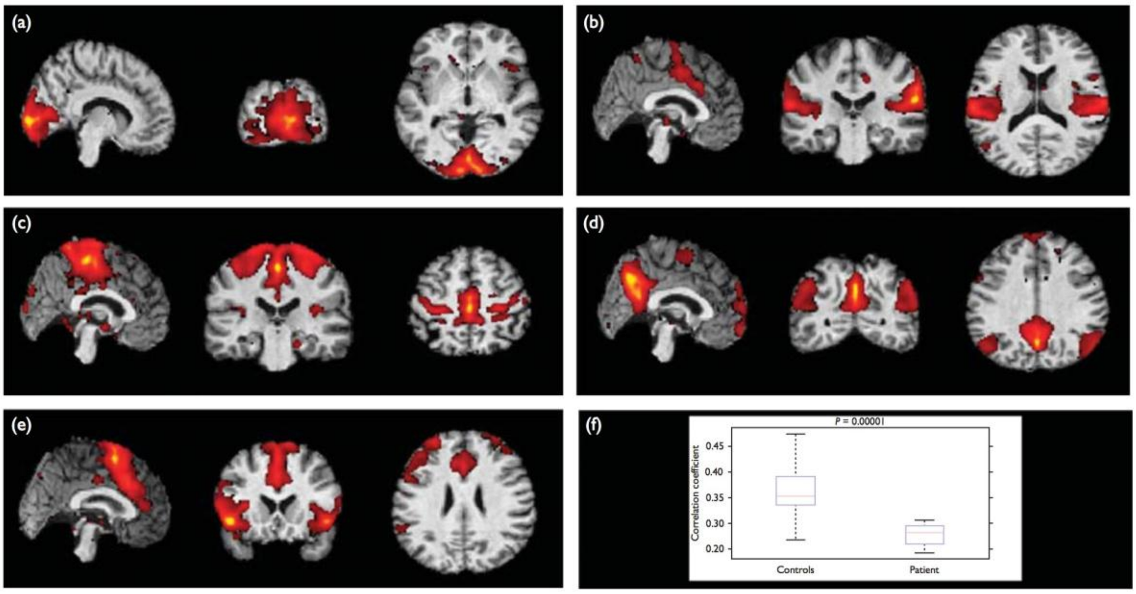

**Figure 35 - Functional MRI: resting-state data. The main functional networks derived from ICA resting-state analysis are shown as red voxels of a highly correlated BOLD signal on the structural T1-weighted volume of the patient. Visual (a), auditory (b), somatosensory (c), default-mode (d), and executive-function (e) networks are clearly recognizable in the patient. The analysis of the correlation's coefficient shows significant differences ($P < 0.001$) between patient and controls (f) only for the executive-function network.**

# Conclusion

The examination of brain BOLD signal by fMRI has led to a revolution in neuroscience over the last decades, producing a lot of papers and scientific research. However, straight-forward BOLD isn’t possible due to the fact that fMRI acquisitions are affected by multiple sources of noise and artifacts. For this reason a lot of preprocess steps are required in the analysis of fMRI datasets. One of the most problematic source of noise is produced by the inhomogeneity of the static magnetic field, which introduces geometric distortions in the images, mainly in the phase-encoding direction. These distortions can heavily affect the correct localization of BOLD activations, in the case of a task-based fMRI, or RSNs, for resting-state fMRI, producing false-positive and false-negative results, both in single an group analysis.

The aim of this thesis was to give an overview of the fMRI data analysis focusing on the correction of the distortions even when corrections are hardly possible due to the lack of support acquisitions. After introducing the problem of EPI spatial distortions, we proposed a new method to correct them based on the acquisition of a T2W 3D volume. This scan can be used to perform a non-linear registration of the EPI to the anatomical reference. In chapter 1, we compared our approach with some of the most used technique to perform such correction, such as FSL TOPUP and FSL FUGUE. Our results suggest that the correction using a T2W as intermediate step provides a good registration of the subjects in the standard space, increasing the significance of the overall activation. We also found an higher percentage of GM active voxel for the proposed approach, compared to the other pipelines. This gave us the means to confirm the goodness of the proposed approach. In chapter 2 we presented our SRA-T1W method, which reconstructs a T2W high resolution isotropic volume form a dataset of T2W 2D acquisition with high in-plane and low through-plane resolution. This volume has many advantages, i.e. performing volumetric analysis with low partial volume effect error, and improving diagnostic possibilities. Our quantitative and qualitative experiments provide a good proof of the validity of the approach. The main advantage of the SRA-T1W method is that it overcomes the problem of the too long acquisition time to obtain an usable T2W isotropic volume, with really high resolution. In the third chapter we also saw how the SRA-T1W can be used to reconstruct a T2W reference for the EPI distortion correction method. This was done to answer to the situation when fMRI dataset are already acquired, with no regards to the EPI distortion correction step. We then compared the combined method with the solution using an acquired T2W volume, and we saw that the two approaches reach quite similar results, confirming the effectiveness of the pipeline. Through the examples described in chapter 4 we finally show the implementation of the proposed method in real clinical studies. Some of these result could not be achieved without correction for EPI distortion.

# References

[1] Williams D. S. et al, “*Magnetic resonance imaging of perfusion using spin inversion of arterial water*”, Proceedings of National Academy of science of USA, vol 89 (1), pag 212-216, Jan 1, 1992;

[2] BR Rosen et al, “*Perfusion imaging with NMR contrast agent*”, Magnetic Resonance in Medicine, vol 14 (2), pag 249-265, May, 1990;

[3] D. Le Bihand et al, “*Diffusion Tensor Imaging: concepts and application*”, Journal of Magnetic Resonance Imaging, vol 13 (4), pag 534-546, Apr, 2001;

[4] T. Tran et al, “*Magnetic resonance spectroscopy in neurological diagnosis*”, Neurologic Clinics, vol 27 (1), pag 21-60, Feb, 2009;

[5] Jeff H. Duyn et al, “*Functional Magnaetic Resonance Neuroimaing Data Acquisition Techniques*”, Neuroimage, vol 4, pag S78-S83, 1996;

[6] J. Henning et al, “*Functional magnetic resonance imaging: a review of methodological aspects and clinical applications*”, vol 18 (1), pag 1-15, Jul 2003;

[7] KJ Friston et al, “*Movement-related effect in fmri time series*”, Magnetic Resonance in Medicine, vol 35 (3), pag 346-355, Mar, 1996;

[8] DH Wu et al, “*Inadequacy of motion correction algorithms in functiona MRI: role of susceptibility-induced artifacts*”, Journal of Magnetic Resonance Imaging, vol 7 (2), pag 365-370, Mar-Apr, 1997;

[9] RM Birn et al, “*Magnetic field changes in the human brain due to swallowing or speaking*”, Magnetic Resonance in Medicine, vol 40 (1), pag 55-60, Jul, 1998;

[10] RM Birn et al, “*Event-related fMRI of task involving brief motion*”, Human Brain Mapping, vol 7 (2), pag 106-114, 1999;

[11] MS Beauchamp, “*Detection of eye movement from fmri data*”, Magnetic Resonance in Medicine, vol 49 (2), pag 376-380, Feb, 2003;

[12] LR Frank et al, “*Estimation of respiration-induced noise fluctuations from undersampled multislice fMRI data*”, Magnetic Resonance in Medicine, vol 45 (4), pag 635-644, Apr, 2001;

[13] G Kruger et al, “*Physiological noise in oxygenation-sensitive magnetic resonance imaging*”, Magnetic Resonance in Medicine, vol 46 (4), pag 631-637, Oct, 2001;

[14] RW Brown et al, “*Magnetic Resonance Imaging: Physical Principles and Sequence Design, Second edition*”, 16 May 2014.

[15] P. Mansfield, “*Multi-planar imaging formation using NMR spin-echo*”, Journal of Physics C: Solid State Physics, vol 10 (3), pag L55-L58, 1977;

[16] RJ Ordidge et al, “*Rapid Biomedical imaging by NMR*”, The British Journal of Radiology, vol 54 (646), pag 850-855, Oct, 1981;

[17] M Poustchi-Amin et al, “*Principles and Applications of Echo-planar imaging: a review for general radiologist*”, Radiographics, vol 21 (3), pag 767-779, May-Jun, 2001;

[18] MJ Stehling et al, “*Whole Body echo planar MR imaging at 0.5 T*”, Radiology, vol 170 (1), Jan, 1989;

[19] P. Mansfield, “*Real-time echo planar imaging by NMR*”, British Medical Bulletin, vol 40 (2), pag 187-190, Apr, 1984;

[20] DA Feinberg et al, “*Echo-planar imaging with asymmetric gradi- ent modulation and inner-volume excitation*”, Magnetic Resonance in Medicine, vol 13 (1), pag 162-169, Jan, 1990;

[21] R. Weisskoff et al, “*Fat suppression techniques: a comparison of results in instant imaging*”, Conference Paper, May, 2017;

[22] GM Bydder et al, “*MR imaging: clinical use of the inversion recovery sequence*”, Journal of Computer Assisted Tomography, vol 9 (4), pag 659-675, Jul-Aug, 1985;

[23] R. Turner et al, “*Passive screening of switched magnetic field gradients*”, Journal of Physics E: Scientific Instruments, vol 19 (10), pag 876, Nov, 2000;

[24] H. Bruder et al, “*Reconstruction procedures for Echo Planar Imaging”,* abstr. 359, 1989;

[25] F. Schmitt et al, “*Useful filterings and phase corrections for EPI derived from a calibration scan*”, Society for Magnetic Resonance Imaging abstr., 464, 1990;

[26] P. Jezzard et al, “*Correction for geometric distortion in Echo Planar Images from B0 Field Variations*”, Magnetic Resonance in Medicine, vol 34 (1), pag 65-73, Jul, 1995;

[27] X. Wan et al, “*Reduction of geometric and intensity distortions in echo-planar imaging using a multireference scan*”, Magnetic Resonance in Medicine, vol 37 (6), pag 932-942, Jun 1997;

[28] H. Chang et al, *“A technique for accurate magnetic resonance imaging in the presence of field inhomogeneities*”, IEEE Transaction on Medical Imaging, vol 11 (3), pag 319-329, 1992;

[29] PS Morgan et al, “*Correction of spatial distortion in EPI due to inhomogeneous static magnetic fields using the reversed gradient method*”, Journal of Magnetic Resonance Imaging, vol 19 (4), pag 499-507, Apr, 2004;

[30] R. Bowtell et al, “*Correction of geometric distortion in echo planar images*”, Book of abstracts: Society of Magnetic Resonance, 2nd Annual Meeting, San Francisco, 6-12 Aug, p 411, 1994;

[31] JL Andersson et al, “*How to correct susceptibility distortions in spin-echo echo-planar images: application to diffusion tensor imaging*”, Neuroimage, vol 20 (2), pag 870-888, Oct, 2003;

[32] J. Kybic et al, “*Unwarping of unidirectionally distorted EPI images*”, IEEE Transaction on Medical Imaging, vol 19 (2), pag 80-93, Feb, 2000;

[33] C. Studholme et al, “*Accurate alignement of functional EPI data to anatomical MRI using a physic-based distortion model*”, IEEE Transaction on Medical Imaging, vol 19 (11), pag 1115-1127, Nov, 2000;

[34] B.B. Avants et al, "*Symmetric diffeomorphic image registration with cross-correlation: Evaluating automated labeling of elderly and neurodegenerative brain*" Medical Image Analysis, vol 12 (1), pag 26-41, 23 Jun, 2007;

[35] J. Kim et al, "*Structural consequences of diffuse traumatic brain injury: A large deformation tensor-based morphometry study*", Neuroimage, vol 39 (3), pag 1014-1026, 1 Feb, 2008;

[36] RN Denison et al., "*Functional mapping of the magnocellular and parvocellular subdivision of human LGN*", Neuroimage, vol 102 (2), pag 358-369, 15 Nov, 2014;

[37] S.M. Smith et al, "*Advances in functional and structural MR image analysis and implementation as FSL*" Neuroimage, vol 23 Supp 1, pag S208-S219, 2004;

[38] B.B Avants et al, "*The Insight ToolKit image registration framework*", Frontiers in Neuroinformatics, 8:44, Apr, 2014;

[39] NJ Tustison et al, "*N4ITK: improved N3 bias field correction*", IEEE Transaction on Medical Imaging, vol 29 (6), pag 1310-1320, Jun, 2010;

[40] M. Jenkinson et al, "*BET2: MR-based estimation of brain, skull and scalp surfaces*" 11th Annual Meeting of the Organization for Human Brain Mapping, 2005;

[41] M. Jenkinson et al, "*Improved Optimisation for the Robust and Accurate Linear Registration and Motion Correction of Brain Images*" Neuroimage, vol 17 (2), pag 825-841, Oct, 2002;

[42] K.J. Friston et al, "*Statistical parametric maps in Functional imaging: a general linear approach*", Human Brain Mapping, vol 2, pag 189-210, 1995;

[43] http://gablab.mit.edu/index.php/software;

[44] B.B Avants et al, "*Geodesic estimation for large deformation anatomical shape averaging and interpolation",* Neuroimage, vol 23 Supp 23, pag S139-S150, 2004;

[45] Y. Zhang et al, "*Segmentation of brain MR images through a hidden Markov random field model and the expectation-maximization algorithm*", IEEE Transaction on Medical Imaging, vol 20 (1), pag 45-57, Jan, 2001;

[46] E.V. Reeth et al, “*Super-resolution in magnetic resonance imaging: a review*” Concepts in Magnetic Resonance, vol 40A (6), pag 306-325, Nov, 2012;

[47] H. Greenspan et al,” *MRI inter-slice reconstruction using super-resolution*”, vol 20 (5), pag 437–446, Jun, 2002;

[48] E. Plenge et al., “ *Super-Resolution reconstruction in MRI: better images faster?*”, in Proc. SPIE Medical Imaging: Image Processing, San Diego, CA, USA, pag 138.1-138.8., 2012;

[49] B. Scherrer et al, “*Super-resolution reconstruction to increase the spatial resolution of diffusion weighted images from orthogonal anisotropic acquisitions*” Medical Image Analysis, vol 16 (7), pag 1465-1476, Oct, 2013;

[50] R. Z. Shilling et al, “ *Sampling strategies for super-resolution in multi-slice MRI*” , in Proc. Image Processing, 15th IEEE International Conference on, San Diego, CA, USA, pag 1465-1476, 2008;

[51] A. Gholipour et al, “*Super-resolution reconstruction in frequency, image, and wavelet domains to reduce through-plane partial voluming in MRI*”, Medical Physics, vol 42 (12), pag 6919-6932, Dec, 2015.

[52] M. Irani et al., “*Super Resolution from image sequences*”, in Proceedings 10th International Conference in Pattern Recognition, Atlantic City, USA, vol 2, pag 115-120, 1990;

[53] M. Irani et al, “*Improving resolution by image registration*”, Graphical Models and Image Processing, vol 53 (3), pag 231-239, May, 1991;

[54] D. Poot et al, “*General and efficient super-resolution method for multi-slice MRI*”, in MICCAI, Berlin/Heidelberg, vol. 6361, pag 615-622Germany, Jan, 2010;

[55] SH. Joshi et al, “*MRI resolution enhancement using total variation regularization*”, Proceedings in IEEE International Symposium on Biomedical Imaging, Boston, MA, USA, pag 161-164, Jun-Jul. 2009;

[56] A. Ben-Ezra et al, “*Regularized super-resolution of brain MRI*”, IEEE International Symposium on Biomedical Imaging, Boston, MA, USA, pag 254-257, Jun-Jul. 2009;

[57] A. Gholipour et al, “*Robust Super-resolution Volume Reconstruction from Slice Acquisitions: Application to Fetal Brain MRI*”, IEEE Transaction on Medical Imaging, vol 29 (10), pag 1739-1758, Jun , 2010;

[58] A. Gholipour et al, “*Maximum A Posteriori Estimation of Isotropic High-Resolution Volumetric MRI from Orthogonal Thick-Slice Scans*”, in MICCAI, vol 6362, pag 109-116, Sep, 2010;

[59] E. Plenge et al, “*Super-Resolution Reconstruction using cross-scale self-similarity in multi-slice MRI*”, MICCAI, vol 16 (pt 3), pag 123-130, 2013;

[60] Y. Iwamoto et al, “*Super-Resolution of MR volumetric images using sparse representation and self-similarity*”, Conference: Pattern Recognition 21st International Conference, 2012;

[61] J. V. Manjón et al, “*MRI Superesolution using self-similarity and Image Priors*”, International Journal of Biomedical Imaging, vol 2010, 12 pag, Oct, 2010;

[62] P. Coupé et al, “*An optimized blockwise non local means denoising filter for 3D magnetic resonance images*”, *IEEE Transaction on Medical Imaging*, vol 27 (4), pag 425-441, Sep, 2008;

[63] A. Buades et al, “*A review of image denoising algorithms, with a new one*”, Multiscale Model and Simulation, vol 4 (2), pag 490-530, 2005;

[64] C. A. Cocosco et al, “*Brain web: online interface to a 3D MRI simulated brain database*”, Neuroimage, vol 5 (4), pag S425, 1997;

[65] D. L. Collins et al, “*Design and construction of a realistic digital brain phantom*”, IEEE Transaction on Medical Imaging, vol 17 (3), pag 463-468, 1998.

[66] AM Coleen et al, “*Williams Syndrome*”, GeneReviews, 23 March, 2017;

[67] CF Beckmann et al, “*Group comparison of resting-state FMRI data using multi-subject ICA and dual regression*”, Organization of Human Brain Mapping, 2009;

[68] F. Arrigoni et al, “*Learning to live without the cerebellum*”, Neuroreport, vol 26 (14), pag 809-813, 30 Sep, 2015;

[69] A. Hyvarien, “*Fast and Robust Fixed-Point Algorithms for Independent component Analysis*”, IEEE Transaction on Neural Networks, vol 10 (3), pag 626-634, 1999;